Resilience assessment of mobile emergency generator-assisted distribution networks: A stochastic geometry approach

Chenhao Ren[a], Rong-Peng Liu[b], Wenqian Yin[a], Qinfei Long[a], Yunhe Hou[a,*]

[a] Department of Electrical and Electronic Engineering, The University of Hong Kong, Hong Kong SAR, China
[b] Department of Electrical and Computer Engineering, McGill University, Montreal QC H3A 0G4, Canada

A B S T R A C T

Escalation of extreme weather events represents substantial threat to power system infrastructure. Mobile emergency generators (MEGs) can form part of a flexible restoration strategy against such destructive events. However, with continued expansion of distribution networks, quantification of the impact of MEGs has become increasingly challenging owing to extreme-weather-event-induced uncertainties. In this paper, we propose a stochastic geometry-based method for assessing the impact of MEG deployment on distribution networks affected by extreme weather events through investigation of structural features. First, we propose a distance measure to represent the electrical connection between power grid components. Subsequently, we adopt the point process and Voronoi tessellation to describe the spatial distribution of power grid components and the service coverage provided by MEGs under different scenarios. Then, we propose a set of assessment metrics to evaluate the survivability of power grid components and the resilience of the entire distribution network under extreme weather events. Finally, we derive accurate analytical expressions for the distance distribution and resilience metrics, such as coverage probability and load shedding, enabling us to explore the relationship between MEG deployment decisions, structural features, and power grid resilience. The proposed method enables analytic assessment of the impact of MEG deployment on the resilience of distribution networks, and provides beneficial insights to help formulate efficient measures for enhancing resilience. Case studies demonstrated that the proposed method is accurate and efficient in dealing with network analysis and assessment problems for distribution networks under massive potential failure scenarios.

1. Introduction

1.1. Background and motivation

Resilient power systems are of paramount importance for ensuring a reliable supply of electricity to a wide range of critical infrastructures (IEA, 2020). However, the resilience of power systems is currently under unprecedented threat owing to increasing climate-change-induced extreme weather events (Busby et al., 2021; McGranaghan et al., 2013). For example, a large-scale power

outage that occurred in Texas (USA), in February 2021, was primarily caused by extremely cold weather. More than 4.5 million residences were affected during the peak outage, causing approximately \$155 billion in losses (Busby et al., 2021). Historical data indicate that approximately 90% of power outages occur in distribution systems (McGranaghan et al., 2013). Therefore, prioritizing the enhancement of distribution system resilience is of utmost importance.

Mobile emergency generators (MEGs), as one type of mobile power equipment, can efficiently enhance the resilience of power grids (Shang et al., 2009). Specifically, they can provide emergency power to support critical loads and serve as a flexible resource for system restoration owing to their mobility and large capacity (i.e., up to several MVA) (Zhou et al., 2009). The potential of MEGs necessitates thorough investigation and exploration because their use offers the prospect for enhanced survivability of critical loads against the impact of extreme weather events. Previous studies mainly focused on a two-stage or a three-stage framework for dispatching MEGs as distributed generators in a distribution network to restore critical loads by forming multiple microgrids (Lei et al., 2018; Wu et al., 2023). In the first stage, MEGs are proactively preassigned to candidate nodes before the occurence of a disaster, whereas in the second stage, MEGs are dispatched in real time after an extreme event has struck (Lei et al., 2018). In Cai et al. (2023), the stage-based uncertainties associated with formulating a two-stage MEG dispatch framework are considered. Reference Wu et al. (2023) considered the resilient operation of distribution systems during disasters and formulated a three-stage MEG dispatch model.

It is noteworthy that extreme weather events pose a substantial challenge in the decision-making process regarding MEG pre-allocation before the occurrence of disasters (Zhang et al., 2021). In highly uncertain extreme weather events, the operation and post-disaster restoration strategies of a power system vary spatiotemporally based on a given predetermine MEG distribution. To address this problem, previous studies investigated power grid outage management under the impact of extreme weather events by considering the co-optimization between MEGs and other crucial response resources such as mobile energy storage systems (Erenog˘lu and Erdinc̦, 2021), distributed generators (Hou et al., 2023), static energy storage systems (Ghasemi and Moshtagh, 2022) and repair crews (Zhang et al., 2023a). However, the impacts of MEG pre-positioning decisions on system resilience, especially power grid structure, have not been well investigated. Specifically, MEG pre-allocation decisions need to consider potential fault scenarios that might arise in a power grid after the occurrence of an extreme event, especially when the failure probability of power grid components is closely related to the intensity of such an event (Wang et al., 2017). Given the vulnerability of the numerous components in a distribution network, such as overhead lines and towers, the number of possible fault scenarios increases rapidly as the scale of the power grid expands. Massive potential failure scenarios pose substantial challenges regarding MEG pre-allocation decisions. Therefore, it is necessary to develop appropriate resilience assessment methods and associated metrics to evaluate the performance of MEG pre-allocation decisions under all potential failure scenarios. In Shafieezadeh and Burden (2014), the macro system performance, such as the average of operation and restoration costs over random distributions of system component failures, was proposed as resilience a assessment metric. Failure scenarios can be generated using a sampling method (Bessani et al., 2019). Accordingly, resilience metrics can be obtained by averaging across all generated scenarios for which the corresponding optimization problems are solved. Nevertheless, this scenario-based method is computationally demanding when assessing large numbers of scenarios, and the optimization problems cannot be solved accurately in polynomial time for large-scale networks. Therefore, it is essential to develop an efficient resilience assessment method for MEG pre-allocation that has acceptable computational complexity.

In addition to MEGs, other structural features of power grids, such as node degree distribution, shortest distance, connectivity, clustering coefficient, and power source distribution, have marked impact on power system resilience. Reference (National Academies of Sciences, 2017) incorporated structural features as constraints in constructing resilience operating strategies. A power grid can be viewed as a complex network (Pagani and Aiello, 2013), and complex network-based analysis methods represent a reasonable approach for analyzing the impact of structural features on resilience. These approaches aim to capture network connectivity features using various centrality indexes, such as node degree and betweenness, and to quantify their ability to sustain basic functions when components fail (Baraba´si, 2013). Centrality indexes reveal inherent properties of networks, such as critical transitions of cascading failures (Scheffer et al., 2012) and demonstrate that network resilience can be determined by low-dimensional network dynamics and topologies (Gao et al., 2016) or by a small set of components (Morone and Makse, 2015). For example, under the impact of extreme weather events, the entire ensemble of power network components and their connections might enhance the overall resilience (Gao et al., 2016). However, existing approaches used to analyze structural features generally only consider network topology and neglect the electric characteristics. Additionally, MEG deployment might potentially influence the structural features of a power grid by resulting in various microgrid formation patterns after the occurrence of an extreme weather event, which is a subject that also requires further research. Therefore, new approaches are urgently needed for systematic assessment of how MEGs and network structural features interact under the impact of extreme weather events and affect power system resilience.

In this paper, we employ stochastic geometry (SG) to develop a comprehensive resilience assessment method for MEG-assisted distribution networks. SG, as an interdisciplinary method combination of geometry and probability theory, is a powerful tool for dealing with random spatial patterns by averaging over all potential geometrical patterns (Chiu et al., 2013). It enables us to analyze the structural features of a network from a novel perspective. By modeling the random locations of network components as spatial point processes, we can analytically derive statistical characteristics of network performance metrics, such as connectivity. SG provides a unified mathematical paradigm for modeling spatial stochastic networks and enables closed-form expressions that describe network behavior. Such expressions facilitate the understanding of network operation and provide insightful design guidelines for network operators, which are often challenging to obtain through computationally intensive simulations (Chiu et al., 2013). The methodology used here has been widely adopted in the study of random phenomena in two-dimensional or higher-dimensional spaces, and it has become a standard tool for modeling and analyzing wireless cellular networks (Andrews et al., 2011). However, few studies have employed SG to address power system problems (Atat et al., 2020a; Atat et al., 2020b). Reference Atat et al. (2020a) proposed a spatiotemporal power grid model based on SG to represent real-world power grids, which enables the implementation of a

multiyear phasor measurement unit allocation scheme. Reference Ren and Hou (2022) proposed an SG-based method to assess the survivability of power transmission systems. In Ren and Hou (2020), Atat et al. (2020b), planning and allocation schemes for electric vehicle charging stations were proposed based on SG. Nevertheless, using SG to assess the impact of MEG deployment on power system resilience remains an unexplored area. In summary, the main research gaps are as follows.

1) The impacts of MEG pre-positioning decisions on power grid structure under massive potential failure scenarios are not fully considered in current two-stage or three-stage MEG deployment frameworks.
2) Scenario-based optimization methods face substantial challenges owing to the high computational costs involved when dealing with massive potential scenarios as power grids expand.
3) The structural features of power grids have not been fully considered, and thus effective and efficient methods are required to address the structural features before and after the impact of extreme weather events.

1.2. Aims and contributions

The main contributions of this paper are summarized below.

1) We propose an SG-based analytical method to assess the performance of MEG deployment decisions in enhancing the resilience of distribution networks against the impact of extreme weather events. First, we employ point processes to depict the spatial distribution of power grid components under various scenarios. Then, Voronoi tessellation is utilized to describe the service coverage of MEGs within the power grids. To the best of the authors' knowledge, this is the first work to employ SG in analyzing the impact of MEGs on power systems.
2) We propose a novel distance measure to characterize the electrical connections between power grid components. Compared with Godsil and Royle (2001), the proposed distance measure considers all potential connection paths between components, and compared with Lagonotte et al. (1989), Poudel et al. (2018), the proposed distance measure is more effective in capturing the changes in electrical connections between components after faults occur. Furthermore, we derive analytical formulations for the distribution functions and expectations of the distance measure to reveal the structural features and to address structure uncertainties within power grids under various failure scenarios. The theoretical formulations accurately align with the actual distance distributions among power grid nodes in various scenarios.
3) We define power system structural resilience for the first time, and we develop a comprehensive framework to analyze structural resilience. A set of assessment metrics is proposed to quantify the structural resilience of distribution networks, and the corresponding analytical results are derived to explore the relationship between structural features, MEG deployment decisions, and structural resilience. Compared with the scenario-based optimization methods, the proposed SG-based method has much higher computational efficiency in analyzing and calculating large-scale networks under massive potential failure scenarios, and the calculation results closely align with the optimization results. The proposed SG-based resilience assessment framework provides beneficial insights for both probabilistic value-based investment planning and appropriate measure selection for efficient enhancement distribution network resilience.

The remainder of this paper is organized as follows. Section II analyzes the structure uncertainty of power grids under the impact of extreme weather events. Section III proposes the SG-based resilience assessment framework for distribution networks. Case studies are presented in Section IV. Finally, our derived conclusions are presented in Section V.

2. Modeling and analysis of structure uncertainty in distribution networks

In this section, we first present the definition and the characterization of structure uncertainty in distribution networks in the face of extreme weather events. Then, we propose a method based on discrete probability distribution to analyze the structure uncertainty from a probabilistic and statistical perspective.

We define the structure uncertainty of a distribution network as the uncertain states of the electrical components (power grid node and power lines), including node types, node injection power, and states of power nodes and power lines after faults occur. For example, when a typhoon passes a specific geographic region, the failure probability of an electrical component within that region is strongly correlated with the intensity and path of the typhoon, thereby resulting in its uncertain state. Uncertain states across multiple components contribute to the structure uncertainty of the entire distribution network. Fig. 1 depicts two possible failure scenarios in a 33-bus distribution network during an extreme weather event. In Fig. 1 (a), line 2–19 and line 10–11 are considered to fail, the impact of which is examined in the case study section. In Fig. 1 (b), line 3–23, line 6–7, and line 32–33 are all considered to encounter faults during an extreme weather event. The relationship between the failure probability of a component and hurricane intensity, proposed in Wang et al. (2017), is expressed as follows:

$$p_{w_t} = \begin{cases} 0 & w_t \leq w_0 \\ \left[1 + \beta \left(\frac{w_t^2}{w_0^2} - 1 \right) \right] \times p_0 & w_0 \leq w_t \leq w_{collapse} \\ 1 & w_t \geq w_{collapse} \end{cases}$$
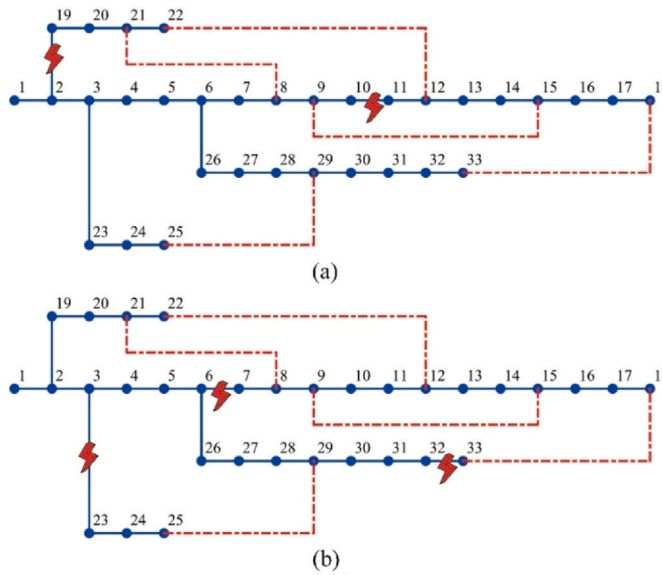
(1)

Fig. 1. Two failure scenarios of a 33-bus distribution network.

where w_t represents the wind speed at time t during the hurricane; p_{w_t} and p_0 correspond to the failure probability of a component under hurricane and normal conditions, respectively; and w_0 and $w_{collapse}$ signify the wind speed thresholds at which a component begins to experience disturbances and damage, respectively. The scaling factor β is determined by the type of weather conditions.

According to (1), the failure probability of a component increases substantially with increase in the intensity of extreme weather events. In the context of a distribution network, high-intensity extreme weather events can cause multiple component failures and alter the network topology. Different numbers and locations of normal and failed components constitute crucial factors in distinguishing failure scenarios, which are referred to as the post-disaster structure patterns of a distribution network. Consequently, when considering multiple components simultaneously, the number of possible post-disaster structure patterns of a distribution network grows exponentially. Specifically, if a power network comprises N components, there will be 2^N failure scenarios because each component has two states, i.e., a normal state and a fault state. The number of post-disaster structure patterns to be addressed for a distribution network with k normal components is expressed as follows:

$$C_N^k = \frac{N!}{k! \times (N-k)!}$$

(2)

Consequently, the computational burden is extremely high, even for a medium-sized distribution network.

One possible approach to address this problem is through the lens of probability and statistics. During an extreme weather event, each electrical component might operate normally with probability p, whereas the probability of failure is $1\text{-}p$, thereby constituting a Bernoulli trial. The state of a component, indicated as y, can be either in normal state denoted by 1 or in fault state represented by 0, following the Bernoulli distribution with parameter p. Assuming homogenous weather conditions across various regions over a short period, all components will experience simultaneous disturbance and share the same failure probability, and the state of each component is deemed independent of that of the others (Panteli et al., 2017). Therefore, the states of N components form a Bernoulli process $\{y_1, y_2, ..., y_N\}$, representing N independent and identically distributed Bernoulli trials. Based on the correlation between the Bernoulli distribution and the binomial distribution (Ross, 2014), the number of components in a normal state after a faults occur can be regarded as a random variable $Y = \sum_{i=1}^{N} y_i$, which follows the binomial distribution, $Y \sim B(N, p)$. Thus, we have the following:

$$\mathbb{P}(Y = k) = C_N^k p^k (1-p)^{N-k}$$

(3)

Equation (3) indicates the proportion of scenarios in which k components operate normally among all possible failure scenarios. The expectation of the number of components operating normally is Np, which assumes a pivotal role in distinguishing various failure scenarios.

The structure uncertainty of a distribution network focuses on the number and location of both normal and failed components, as well as on their connections, during extreme weather events. Instead of assessing a specific scenario and calculating a concrete resilience assessment metric, this paper investigates scenarios of multiple component failures and derives their statistical characteristics relevant to resilience, e.g., the expected value and probability distribution of resilience metrics. Our aim is to propose an effective method for modeling and analyzing the structure uncertainty of a distribution network under the impact of extreme weather events in a probabilistic manner.
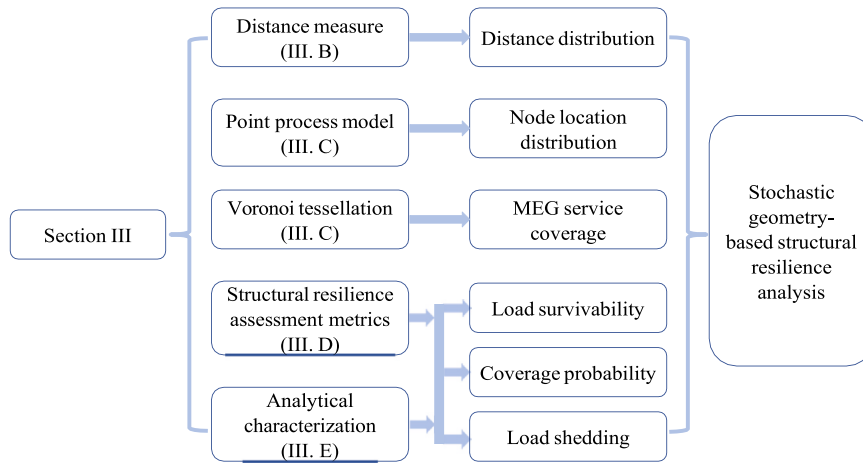
Fig. 2. Framework of the proposed method.

3. Stochastic geometry-based resilience assessment method

In this section, we propose an SG-based approach for evaluating the performance of various MEG deployment decisions while considering the structure uncertainty induced by extreme weather events. We first provide a comprehensive overview of SG and point process theory. Subsequently, we propose a distance measure to describe the connection among power grid nodes. Moreover, we define the structural resilience of a power system and propose a novel point process model to characterize possible locations of power grid nodes in different scenarios. To illustrate the service coverage of MEGs, we employ a Voronoi tessellation-based method. Finally, we develop effective metrics to evaluate the structural resilience and to derive analytical expressions to quantify the structural resilience of a distribution network under the impact of extreme weather events. The framework depicted in Fig. 2 outlines the structure of Section III.

3.1. Preliminaries of stochastic geometry and point process

The SG method is a branch of applied probability theory that deals with the study of random spatial patterns. At its core, point processes serve as fundamental and pivotal subjects of investigation. SG provides a powerful tool for depicting a random collection of points in both one-dimensional and multi- dimensional space, enabling computation of statistical averages over all possible realizations of a point process. This proficiency empowers us to extract comprehensive performance analyses, establish guiding principles, and obtain invaluable design insights (Haenggi, 2012).

In this paper, we focus on the functionality of individual electrical components and on the average functionality exhibited by all electrical components across all possible failure scenarios of a distribution network under the impact of extreme weather events. Specifically, we employ point processes to model the spatial distribution of the components, the different realizations of which characterize the possible locations of the components under different scenarios. Those realizations correspond to the random spatial patterns of the distribution network. Subsequently, we analytically derive the statistical properties characterizing the random spatial patterns of a distribution network by employing tools from SG.

For clarity, we first give a detailed definition of point processes.

Definition 1. (Point Process) (Haenggi, 2012): Considering a Euclidean space $\mathbb{R}^d$, a point process $\Phi = \{x_i, i \in \mathbb{N}\}$ is a finite and countable random collection of points residing in $\mathbb{R}^d$.

Remark: Φ is a countable random set consisting of random variables $x_i \in \mathbb{R}^d$ as its elements. Φ can also be defined by the random measure formalism, which counts the number of points falling in a Borel set $B \subset \mathbb{R}^d$ Haenggi (2012), defined as

$$\psi(B) = \sum_{x \in \Phi} \delta_x \, (x \in B)$$

(4)

where $\delta_x(B) = \mathbf{1}_B(x)$ is the Dirac measure at point x. Here, $\delta_x(B) = 1$ if $x \in B$, $\delta_x(B) = 0$ if $x \notin B$.

Definition 2. (Poisson Point Process) (Haenggi, 2012): If a point process Φ satisfies the following conditions:

i) the number of points falling into any compact Borel set $B \subset \mathbb{R}^d$, i.e., $\psi(B)$ follows the Poisson distribution,

$$\mathbb{P}\left[\psi(B) = n\right] = e^{-\lambda v_d(B)} \frac{[\lambda v_d(B)]^n}{n!}$$

(5)

where λ denotes the intensity density of Φ. Here, λ describes the average number of points falling into the unit space, and $v_d(B)$ denotes the Lebesgue measure of Borel set B.
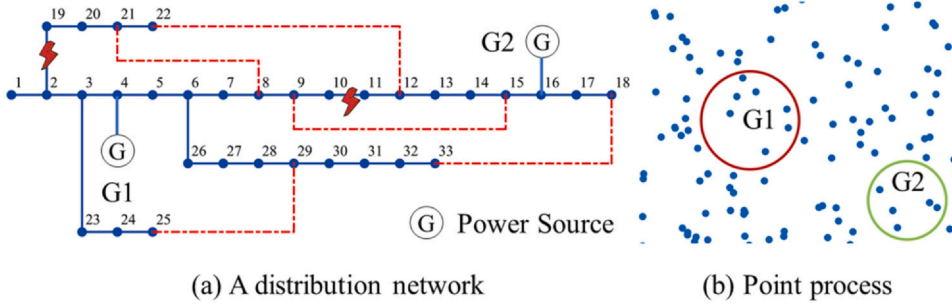
Fig. 3. A power network and its point process realization.

ii) $\psi(B_1)$, $\psi(B_2)$, … $\psi(B_m)$ are independent variables if B_1, B_2, $B_{3,}$. B_m are disjoint bounded sets in $\mathbb{R}^d$. Then, point process Φ is a Poisson point process.

This paper maps the distribution network into a point process. Fig. 3(a) illustrates a distribution network with two power sources, and Fig. 3(b) shows a realization of the corresponding point process on a plane. The bounded sets G_1 and G_2 represent the coverage areas of the power source G_1 and G_2, respectively. Points falling into bounded sets G_1 and G_2 represent the load consumers supplied by the respective power source, whereas points located outside of sets G_1 and G_2 denote load consumers that cannot be served by MEGs. The proposed approach leveraging the point process considers all possible scenarios by mapping them onto corresponding realizations of the point process. Consequently, we can derive the average performance of power source deployment decisions by averaging over all potential realizations of the point process, thereby furnishing a groundbreaking perspective for tackling a multitude of scenarios.

3.2. Distance measure between power grid nodes

Apart from modeling location distributions of power grid nodes, it is crucial to accurately quantify their interconnections. We propose a distance measure that precisely quantifies the electrical connections among power grid nodes.

For a given power network, consider the injection of unit current into node i and the extraction of unit current from node j, with all other nodes remaining as open circuits. By applying the power network equation $\boldsymbol{I} = \boldsymbol{Y}\boldsymbol{V}$ and Kirchhoff's law, we can express the current difference $\boldsymbol{i} = \boldsymbol{e}_i - \boldsymbol{e}_j = \boldsymbol{Y}\boldsymbol{v}$, where $\boldsymbol{i}$, $\boldsymbol{v} \subset \mathbb{R}^d$ represent the current vector and the voltage vector, respectively (Song et al., 2019). Consequently, the voltage difference between node i and node j can be expressed as follows:

$$v_i - v_j = (\boldsymbol{e}_i - \boldsymbol{e}_j)^{\mathrm{T}}\boldsymbol{v} = (\boldsymbol{e}_i - \boldsymbol{e}_j)^{\mathrm{T}}\boldsymbol{Y}^{\dagger}(\boldsymbol{e}_i - \boldsymbol{e}_j) \tag{6}$$

As depicted in (6), this voltage difference arises from the different current injections of node i and node j. Accordingly, we define the distance measure between node i and node j as follows.

Definition 3. (Distance Measure between Power Grid Nodes): The distance measure between any pair of node i and node j in a power network is defined as follows:

$$r_{ij} = (\boldsymbol{e}_i - \boldsymbol{e}_j)^{\mathrm{T}}\boldsymbol{Y}^{\dagger}(\boldsymbol{e}_i - \boldsymbol{e}_j) \tag{7}$$

where $\boldsymbol{Y}^{\dagger}$ is the pseudo inverse of $\boldsymbol{Y}$, $\boldsymbol{e}_i$, $\boldsymbol{e}_j \subset \mathbb{R}^n$.

Remark. The proposed distance measure has clear physical meaning. It should be emphasized that a smaller r_{ij} signifies a reduced voltage difference and a more robust link between node i and node j. In terms of voltage support, when node i is connected to a power source and node j connects a load consumer, supplying power to the load consumer generates a voltage drop in the power source. If the voltage drop exceeds the voltage limit, it signifies that the power source cannot support or cover this load. Hence, the distance reflects both the level of difficulty a load consumer encounters in obtaining power from a power source and the priority level of supplying a power source to the load consumer, when considering the maintenance of voltage stability.

Additionally, unlike other distance metrics, such as the topological distance determined by the shortest path length between nodes (Godsil and Royle, 2001), the proposed distance measure accommodates all parallel paths linking the nodes. In summary, by employing the proposed distance measure, we can effectively quantify the electrical connection between any two nodes within a power network. Furthermore, using the derived distance distributions in Section III. E, we can quantitatively assess any changes in the connection between nodes caused by extreme weather events.

3.3. Coverage characterization of MEGs based on point process and voronoi tessellation

1) Point process model of distribution networks: In this part, we first provide a definition of the structural resilience of a power network. The structural resilience of a power network focuses on managing resilience from the perspective of network structure. It

considers not only the network topology but also the topological statistical indexes encompassing connectivity and connection between power grid nodes, as well as certain statistics of electrical structural features, such as the spatial distribution and sizing of power sources, load consumers, and external flexible resources. Specifically, it characterizes resilience through statistical structural feature.

As indicated previously, extreme weather events induce changes in the connections among power grid nodes and network connectivity, leading to uncertainty in the overall structure and introducing risk to the structural resilience of a power network. To address the structure uncertainty, we propose a point-process-based method that models the spatial locations of power grid nodes, enabling diverse realizations that depict possible node locations. Consequently, when the point process model is ergodic, all possible spatial locations are implemented, allowing probabilistic analysis of the power network's average performance.

Distribution networks equipped with external flexibility resources, e.g., MEGs, mobile energy storage, and distribution generation units, are referred to as heterogeneous distribution networks. The deployment of MEGs has notable impact on the structure of a distribution network, amplifying its complexity and heterogeneity, especially during and after the occurrence of extreme weather events. To establish a comprehensive and cohesive point process model for heterogeneous distribution networks, we employ multiple spatially coexisting tiers. Each tier is characterized by distinct types of flexibility resources, varying numbers of resources, and capacity. In this paper, we focus solely on the deployment of MEGs. The critical aspects of the proposed point process model can be summarized as follows:

i) MEGs are modeled by a Poisson point process Φ_G with intensity density λ_G;
ii) Load consumers are modeled by a point process Φ_u with intensity density λ_u;
iii) The power consumption of any load consumer is less than the maximum output power of any MEG.

To implement the aforementioned point process model, we design an algorithm, shown in Algorithm 1, which generates points in a plane-domain subject to the Poisson point process.

Algorithm 1. A plane-domain generation method for a Poisson point process.

1: **Input** $\{r_1, r_2, \ldots, r_s\}$, λ_1, λ_2, **initialize** i=1;
2: **while** $i \leq s$, **do**
3:         Generate circle $C \equiv \{(x, y): x^2 + y^2 \leq r^2\}$;
4:         Generate the number of points: $N_1 \sim Poisson(\pi\lambda_1 r_i^2)$, set $N \leftarrow N_1$;
5:         **If** N=0 **then** exit; otherwise generate independent: $u_k \sim U(0,1)$, k=1, 2, … N;
6:         Set $\rho_k \leftarrow r_i\sqrt{u_k}$, k=1, 2, … N;
7:         Sort $\rho_1, \rho_2, \ldots \rho_N$ in ascending order, obtain $\tilde{\rho}_1, \tilde{\rho}_2, \ldots \tilde{\rho}_N$;
8:         Generate independent $v_k \sim U(0,1)$, k=N+1, N+2, … 2N;
9:         Set $\theta_1 \leftarrow 2\pi v_{N+1}$, $\theta_2 \leftarrow 2\pi v_{N+2}$, …$\theta_n \leftarrow 2\pi v_{2N}$;
10:        Obtain $(\tilde{\rho}_1, \theta_1), (\tilde{\rho}_2, \theta_2), \ldots (\tilde{\rho}_{N_1}, \theta_{N_1})$;
11:        Generate the number of points: $N_2 \sim Poisson(\pi\lambda_2 r_i^2)$;
12:        Set $N \leftarrow N_2$, perform step(4) - step(8);
13:        Obtain $(\tilde{\rho}_1, \theta_1), (\tilde{\rho}_2, \theta_2), \ldots (\tilde{\rho}_{N_2}, \theta_{N_2})$;
14:        i=i+1, go to step 2;
15: **end while.**

Theorem 1 provides theoretical support for Algorithm 1.

Theorem 1. Suppose $(\rho_1, \theta_1), (\rho_2, \theta_2), \ldots (\rho_N, \theta_N)$ are polar coordinates of $N > 0$ points from a Poisson point process on the circle $C \equiv \{(x, y): x^2 + y^2 \leq r^2\}$, and $\rho_1, \rho_2, \ldots \rho_N$ are sorted in ascending order, denoted by $\tilde{\rho}_1, \tilde{\rho}_2, \ldots \tilde{\rho}_N$. Then the ordered radii $\tilde{\rho}_1, \tilde{\rho}_2, \ldots \tilde{\rho}_N$ are order statistics. The probability density function of the order statistic $\tilde{\rho}_k$ is $f_{\tilde{\rho}_k}(x) = \frac{2x}{r^2}$, $x \in [0, r]$. Here, $\theta_1, \theta_2, \ldots \theta_N$ are independent and identically distributed on $[0, 2\pi]$.

Proof According to the definition of order statistics (David and Nagaraja, 2004), the ordered radii $\tilde{\rho}_1, \tilde{\rho}_2, \ldots \tilde{\rho}_N$ are order statistics. The probability density function of $\tilde{\rho}_k$ is denoted as $f_{\tilde{\rho}_k}(x)$, and the distribution function of $\tilde{\rho}_k$ is denoted as $F_{\tilde{\rho}_k}(x)$. The calculation formula for $f_{\tilde{\rho}_k}(x)$, based on the probability density elements, is expressed as follows:

$$f_{\tilde{\rho}_x}(x) = \lim_{\Delta x \to 0} \frac{\mathbb{P}(x < \tilde{\rho}_x \leq x + \Delta x)}{\Delta x} \tag{8}$$

where $\mathbb{P}(x < \tilde{\rho}_k < x + \Delta x)$ represents the probability of any point falling into a circle with an inner circle radius of x and an outer circle radius of $x + \Delta x$. We know that $\mathbb{P}(x < \tilde{\rho}_k < x + \Delta x) = \frac{2x\Delta x}{r^2}$. Therefore, the probability density function $f_{\tilde{\rho}_k}(x) = \frac{2x}{r^2}$, $x \in [0, r]$.

Here, $\theta_1, \theta_2, \ldots \theta_N$ are not order statistics. According to the definition of the Poisson point process, $\theta_1, \theta_2, \ldots \theta_N$ are independent and identically distributed on $[0, 2\pi]$.

This completes the proof. $\square$.

2) Coverage characterization of MEGs based on Voronoi tessellation: To accurately depict the service coverage of MEGs concerning load consumers in response to potential extreme weather events, we employ Voronoi tessellation. Mathematically, this tessellation is created by a series of randomly scattered points on a plane. For every point within point process Φ, the associated Voronoi cell is defined as follows:

$$C_k = \{a \in \Phi | r(a, x_k) < r(a, x_j), j \neq k\} \tag{9}$$

where $r(a, x_k)$ represents the distance between node a and node x_k.

In this paper, the distances between nodes based on the proposed distance measure serve as the numerical measures for computing the Voronoi tessellation. Mathematically, a measurable mapping from the probability space to the measurable space is referred to as a point process. By employing the proposed distance measure as the measure of this measurable space, the distance between any two points in the point process can be obtained, representing the mapping of electrical connections between power grid nodes in the measurable space. Additionally, this paper considers the problem of the decision regarding MEG deployment in a power grid before extreme-event-induced faults occur, but it does not involve real-time MEG-scheduling issues during and after the occurrence of extreme events. In practical situations, the gathering locations of MEGs might not coincide with the geographical locations of power grid nodes, but they will not be too far away from each other to respond quickly to faults. For simplification, this paper assumes that MEGs are deployed at the geographical locations of power grid nodes, enabling them to access the power grid at any time. Therefore, the physical distances between MEGs are converted to the distances between those power grid nodes equipped with MEGs, which can be quantified using the distance measure proposed in this paper.

By utilizing the coordinates calculated through Algorithm 1 and the distances between nodes, we leverage the Bowyer-Watson algorithm proposed in (Watson, 1981) to generate the Voronoi tessellation, effectively dividing the network into multiple Voronoi cells. The distribution of MEGs and load consumers presented in Fig. 4, together with the coverage of MEGs on load consumers, provides visual representation of how the proposed approach based on the Poisson point process and Voronoi tessellation works. The polygons enclosed by the black solid lines in Fig. 4, called Voronoi cells, represent the coverage range of the MEGs within the associated cells. For any specific MEG, the load consumers residing within its Voronoi cell can be supplied by the MEG, indicating that those load consumers can be covered by the MEG. Conversely, load consumers located outside of the Voronoi cell of any specific MEG are covered by other associated MEGs. The proposed Poisson point process model is leveraged to describe the potential spatial distribution of MEGs and load consumers in the power grid across various scenarios, including both normal and fault conditions. By employing the proposed distance measure as a metric, the relative positional distribution of MEGs and MEGs/load consumers is mapped in the metric space. Then, Voronoi tessellation is utilized to determine the service coverage of each MEG, signifying its coverage of neighboring load consumers. The integration of the Poisson point process with Voronoi tessellation represents a method for analysis and computation of the coverage of MEGs on load consumers in specific scenarios. Through different realizations of the Poisson point process in distance metric space, followed by the utilization of Voronoi tessellation, the coverage range of each MEG can be obtained, effectively describing the power supply situation of MEGs to load consumers across diverse scenarios.

3.4. Structural resilience assessment considering MEG deployment

In this subsection, we formulate a comprehensive set of evaluation metrics to assess the structural resilience of a distribution network, specifically focusing on load survivability, coverage probability, and load shedding.
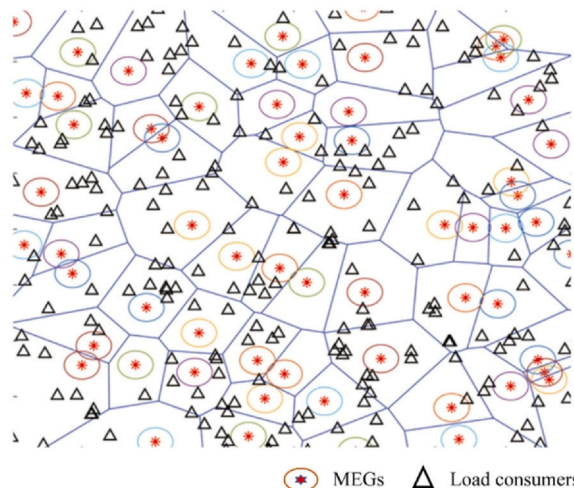

Fig. 4. Poisson distributed MEGs, with each load associated with the nearest MEG.

As a starting point, we propose a load survivability metric that effectively captures the ability of load consumers to withstand extreme weather events. We divide the set of nodes in the power grid into two sets: N_L, representing the load consumers, and N_G, representing the nodes allocated with MEGs.

Definition 4. (Load Survivability): The load survivability metric SI_i for load consumer $i \in N_L$ is defined as follows:

$$SI_i = \frac{\omega_i \frac{P_{G_j}}{P_{L_j}} \left(\min_{j \in N_G} r_{ij} \right)^{-\alpha}}{\sum_{k \in N_G, k \neq j} \frac{P_{G_k}}{P_{L_i}} (r_{ik})^{-\alpha}}$$

(10)

where ω_i signifies the priority of load consumer i. P_{L_i} represents the active power consumption of load consumer i, and P_{G_j} represents the upper limit of the active power output of the MEG located at node j. Furthermore, r_{ij} denotes the distance between load consumer i and MEG node j, and α serves as a coefficient that quantifies the weight of power consumption for load consumers together with their distances to the nearest MEG. Equation (10) precisely characterizes the ease with which a load consumer can obtain power from its nearest MEG during an extreme weather event without compromising the survivability of other consumers. By combining (7) and (10), we can derive the following:

$$SI_i = \frac{\omega_i \frac{P_{G_j}}{P_{L_i}} \left[\min_{j \in N_G} \left\{ \left(\mathbf{e}_i - \mathbf{e}_j \right)^T \mathbf{Y}^\dagger \left(\mathbf{e}_i - \mathbf{e}_j \right) \right\} \right]^{-\alpha}}{\sum_{k \in N_G, k \neq j} \frac{P_{G_k}}{P_{L_i}} \left[\left(\mathbf{e}_i - \mathbf{e}_k \right)^T \mathbf{Y}^\dagger \left(\mathbf{e}_i - \mathbf{e}_k \right) \right]^{-\alpha}}$$

(11)

Equation (11) establishes the relationship between the power network structure (admittance matrix $\mathbf{Y}$), MEG parameters, and the survivability of load consumers.

Our proposed methodology adheres to the principle of maximizing coverage by leveraging available flexibility resources to support loads to the greatest extent possible. Considering the uncertainties in network structure caused by extreme weather events, pre-positioned MEGs might not align perfectly with the requirements of each outage area. Therefore, we propose the concept of coverage probability to evaluate the survivability of both the load consumers and the entire network following the proactive positioning of MEGs at various candidate nodes.

Specifically, the coverage probability is equivalent to the following:

  i) The probability that a random load consumer achieves a target survivability threshold or
 ii) The average fraction of load consumers satisfying the target survivability threshold at any specific time or
iii) The average fraction of an area in the network that is "in coverage" at any time.

Definition 5. (Coverage Probability for Power Grid Nodes): The coverage probability for power grid node i is defined as follows:

$$p_{cov,i} = \mathbb{P}\left[SI_i > T \right]$$

(12)

where T represents the survivability threshold for power grid nodes. A load being "in coverage" indicates that its survivability exceeds threshold T. The value of T can be an adjustable parameter or the maximum failure probability of electrical components.

Definition 6. (Coverage Probability of Power Grids): The coverage probability for power grids is defined as.

$$p_{cov,sys} = \mathbb{E}_r\left[\mathbb{P}\left(SI > T | r \right) \right]$$

(13)

Equation (13) captures the macro performance of a power grid, revealing the average survivability of the power grid nodes during the occurrence of extreme weather events after the MEGs have been pre-positioned.

Definition 7. (Load Shedding of Power Grids): The load shedding of power grids under MEG deployment is defined as.

$$LS_{sys} = (1 - p_{cov,sys}) \sum_{i \in N_L} P_{L_i}$$

(14)

where $\sum_{i \in N_L} P_{L_i}$ represents the total load consumption in a power grid.

By analyzing (10)-(14), we can gain insights into the macro-level performance of a power grid under different MEG deployment strategies, thereby offering valuable theoretical decision-making guidance for system operators. The detailed analytical expressions of (12)-(14) are derived in Section III. E.

3.5. Analytical characterization of power grid structural resilience

This part derives analytical results for the distance distributions between power grid nodes and the structural resilience metrics of a power grid.

1) *Distance distribution between power grid nodes:* In Section III. B, we propose a distance measure to quantify the electrical connection between power grid nodes. Distance is a crucial factor separating a specific node from other nodes. Owing to the impact of severe

weather events on power grid nodes and power network structures, the distances between nodes become stochastic under different failure scenarios. Let r_i, $i = 1, 2, ...n$ represent a set of random variables indicating distances from a randomly chosen node to its n-th nearest neighbor. Our focus lies in obtaining the probability distribution form of the random variable r_i. For the sake of convenience and generality, we assume that this randomly chosen node and the other nodes can be considered homogeneous, and that the analysis results obtained based on this node are general and can represent the characteristics of other nodes in the power grid, as well as describe the overall characteristics of all nodes in the power grid. The distribution function of r_n, which denotes the distance from the randomly chosen node to its n-th nearest neighbor, is denoted as $F_{r_n}(R)$. We now provide the analytical descriptions for $F_{r_n}(R)$.

Theorem 2. In a power grid with $n + 1$ nodes, the distance between any node and its n-th nearest neighboring node is represented as r_n. The distribution function of r_n is given by the following:

$$F_{r_n}(R) = 1 - e^{-\lambda \pi R^2} \sum_{k=0}^{n-1} \frac{(\lambda \pi R^2)^k}{k!} \tag{15}$$

where λ represents the proportion of non-island nodes in the power grid.

Proof Assuming that the location distribution of nodes in a power grid can be described by Poisson point process Φ with density intensity λ, representing the proportion of non-island nodes in the power grid. The probability of k points from Φ falling into a bounded closed set B in d-dimensional Euclidean space $\mathbb{R}^d$ is as follows:

$$\mathbb{P}(\psi(B) = k) = e^{-\lambda v_d(B)} \frac{[\lambda v_d(B)]^k}{k!} \tag{16}$$

where $v_d(B)$ denotes the Lebesgue measure of bounded closed set B, which corresponds to the area when considering a two-dimensional plane.

Assuming that the randomly chosen node is located at origin o on the plane. Because the points of the point process are distributed uniformly on the plane (and in higher dimensions), the shape of the closed set B on the plane is circular. When there are k points in B, the radius of B is equal to the distance from the randomly chosen node to the k-th nearest point. Hence, the measure of the closed set B is πr^2.

The number of points in closed set B, i.e., $\psi(B)$ is a discrete random variable. For the probability that $\psi(B) < n$ is equivalent to the sum of the probabilities that $\psi(B) = 1, 2,. n - 1$, we have the following: :

$$\mathrm{P}\left(\psi\left(B\left(o, r_n\right)\right) < n\right) = \sum_{k=0}^{n-1} e^{-\lambda \pi r_k^2} \frac{\left(\lambda \pi r_k^2\right)^k}{k!} \tag{17}$$

Equation (17) precisely represents the complementary cumulative distribution function of r_n. Specifically, the cumulative distribution function of r_n gives $\mathrm{P}(r_n \leq R)$. Its complementary cumulative distribution function is given by $1 - \mathrm{P}(r_n > R)$. Here, $\mathrm{P}(r_n > R)$ represents the probability that the distance from the randomly chosen node to its n-th nearest neighbor is greater than R. This is equivalent to the probability that there are at most $n - 1$ nodes within a circle of radius R centered at the chosen node. Therefore, we have the following:

$$
\begin{aligned}
F_{r_n}(R) &= \mathrm{P}(r_n \leq R) = 1 - \mathrm{P}(r_n > R) = 1 - \mathrm{P}\left(\psi\left(B(o, R)\right) < n\right) \\
&= 1 - e^{-\lambda \pi R^2} \sum_{k=0}^{n-1} \frac{\left(\lambda \pi R^2\right)^k}{k!}
\end{aligned}
\tag{18}
$$

This completes the proof. □

Based on Theorem 2, we can derive the following propositions and corollaries.

Proposition 1. In a power grid with $n + 1$ nodes, the probability distribution function of the distance between any node and its n-th nearest node is as follows:

$$f_{r_n}(r) = \frac{2(\lambda \pi)^n}{\Gamma(n)} r^{2n-1} e^{-\lambda \pi r^2} \tag{19}$$

where $n = 1, 2,..$ $\Gamma(n)$ denotes the standard gamma function defined as $\Gamma(n) = \int_0^\infty t^{n-1} e^{-t} dt$, and λ denotes the proportion of non-island nodes in the power grid.

Proof By utilizing the cumulative distribution function of r_n, we can determine the probability distribution function of r_n as follows:

$$
\begin{aligned}
f_{r_n}(r) &= \frac{\mathrm{d}F_{rn}(r)}{\mathrm{d}r} \\
&= 2\lambda\pi r e^{-\lambda\pi r^2} \sum_{k=0}^{n-1} \frac{(\lambda\pi r^2)^k}{k!} - e^{-\lambda\pi r^2} \sum_{k=0}^{n-1} 2\lambda\pi r \frac{(\lambda\pi r^2)^{k-1}}{(k-1)!} \\
&= \frac{2(\lambda\pi)^n}{\Gamma(n)} r^{2n-1} e^{-\lambda\pi r^2}.
\end{aligned}
\tag{20}
$$

This completes the proof. $\square$

Corollary 1. The probability distribution function of the nearest distance r_1 separating any node from its nearest node is given by.

$$
f_{r_1}(r) = 2\lambda\pi r e^{-\lambda\pi r^2}
\tag{21}
$$

where λ denotes the proportion of non-island nodes in the power network.

Proof (21) can be obtained by taking n as 1 in (19). This completes the proof $\square$

Proposition 1 and Corollary 1 provide the probability density function of the distance from any node to its n-th nearest node in the power grid. The analysis of distance distributions assists in both revealing the inherent structures of power grids and assessing the structural resilience under various extreme events. In a power grid with distributed generators, such results are helpful for analyzing the distribution characteristics of distances between load consumers and generators at different locations within the power grid.

Considering that each load consumer tends to obtain power from its nearest power source owing to the small loss, Corollary 1 provides a quantitative description of the distance distribution from any load consumer to its nearest generator. This information is valuable for making decisions regarding the deployment of MEGs. Proper deployment of MEGs can effectively improve the distribution of distances between load consumers and their nearest generators in the power grid, thereby enhancing the expected survivability of load during extreme events.

Proposition 2. In a power grid with $n + 1$ nodes, the expectation of the distance from any node to its n-th nearest neighboring node is as follows:

$$
\mathbb{E}(r_n) = \frac{(2n-1)!!}{2^n \Gamma(n)\sqrt{\lambda}}
\tag{22}
$$

where λ denotes the proportion of non-island nodes in the power network.

Proof Using the probability density function of r_n shown in (19), we can derive the expectation of r_n

$$
\begin{aligned}
\mathbb{E}(r_n) &= \int_{-\infty}^{+\infty} r \cdot \frac{2(\lambda\pi)^n}{\Gamma(n)} r^{2n-1} e^{-\lambda\pi r^2} \mathrm{d}r \\
&= \frac{2(\lambda\pi)^n}{\Gamma(n)} \int_0^{+\infty} r^{2n} e^{-\lambda\pi r^2} \mathrm{d}r
\end{aligned}
\tag{23}
$$

Denoting $I_n = \int_0^\infty r^{2n} e^{-\lambda\pi r^2} \mathrm{d}r$, we have the following

$$
\begin{aligned}
I_n &= \frac{2n-1}{2\lambda\pi} \int_0^{+\infty} r^{2n-2} e^{-\lambda\pi r^2} \mathrm{d}r \\
&= \frac{2n-1}{2\lambda\pi} I_{n-1}
\end{aligned}
\tag{24}
$$

Utilizing the recursive formula of integral I_n, we can obtain the expression shown below.

$$
\begin{aligned}
\mathbb{E}(r_n) &= \frac{2(\lambda\pi)^n}{\Gamma(n)} I_n \\
&= (\lambda\pi)^{n-1} \frac{2n-1}{\Gamma(n)} I_{n-1} \\
&= \frac{(2n-1)!!}{2^n \Gamma(n)\sqrt{\lambda}}
\end{aligned}
\tag{25}
$$

where $\Gamma(n) = (n-1)!$ for $n \in \{1, 2, ...\}$.

This completes the proof. $\square$

Corollary 2. The expectation of the distance from any node to its nearest node in the power grid is.

$$
\mathbb{E}(r_1) = \frac{1}{2\sqrt{\lambda}}
\tag{26}
$$

where λ denotes the proportion of non-island nodes in the power network.

Proof (26) can be obtained by taking n as 1 in (22). This completes the proof $\square$

Proposition 3. In a power grid with $n + 1$ nodes, the second origin moment of the distance between any node and its n-th nearest neighboring node is as follows:

$$\mathbb{E}(r_n^2) = \frac{n(n+1)}{(\lambda\pi)^2}$$

(27)

where λ denotes the proportion of non-island nodes in the power grid.

Proof We can derive the distribution function of r_n^2 using (15):

$$\mathbb{P}(r_n^2 \le R) = F_{r_n}(\sqrt{R}) = 1 - e^{-\lambda\pi R}\sum_{k=0}^{n-1}\frac{(\lambda\pi R)^k}{k!}$$

(28)

Hence, the probability density function of r_n^2 can be determined as follows:

$$f_{r_n^2}(r) = \frac{(\lambda\pi)^n r^{n-1}e^{-\lambda\pi r}}{\Gamma(n)}$$

(29)

By applying the definition of the second origin moment for a random variable, we have the following:

$$\begin{aligned}\mathbb{E}(r_n^2) &= \int_0^\infty r^2 \cdot \frac{(\lambda\pi)^n r^{n-1}e^{-\lambda\pi r}}{\Gamma(n)}\mathrm{d}r \\ &= \frac{(\lambda\pi)^n}{\Gamma(n)}\int_0^\infty r^{n+1}e^{-\lambda\pi r}\mathrm{d}r\end{aligned}$$

(30)

Denoting $I_{n+1} = \int_0^\infty r^{n+1}e^{-\lambda\pi r}\mathrm{d}r$, we have the following:

$$\begin{aligned}I_{n+1} &= \int_0^\infty r^{n+1}e^{-\lambda\pi r}\mathrm{d}r = \frac{n+1}{\lambda\pi}\int_0^\infty r^n e^{-\lambda\pi r}\mathrm{d}r \\ &= \frac{n+1}{\lambda\pi}I_n\end{aligned}$$

(31)

Based on the recursive formula of integral I_{n+1}, we can obtain the following:

$$\begin{aligned}\mathbb{E}(r_n^2) &= \frac{(\lambda\pi)^n}{\Gamma(n)}I_{n+1} = \cdots = \frac{(\lambda\pi)^n}{\Gamma(n)} \cdot \frac{(n+1)!}{(\lambda\pi)^n}I_1 \\ &= \frac{n(n+1)}{(\lambda\pi)^2}\end{aligned}$$

(32)

This completes the proof. □

Corollary 3. The second origin moment of the distance between any node and its nearest node in the power grid is.

$$\mathbb{E}(r_1^2) = \frac{2}{(\lambda\pi)^2}$$

(33)

where λ denotes the proportion of non-island nodes in the power grid.

Proof (33) can be obtained by taking n as 1 in (27). This completes the proof.□

Proposition 2, Corollary 2, Proposition 3, and Corollary 3 quantify the average distances and the degree of dispersion of distance from all nodes to their n-th neighbor nodes. It can be observed that an increased number of non-island nodes markedly reduces the average distance between nodes. In other words, extreme weather events that cause component failures lead to increase in the distance between nodes in a power grid because there are more isolated nodes.

2) *Coverage probability:* We now present our analytical results regarding the coverage probability of load consumers in a power grid.

Theorem 3. In a power grid with N_L load consumers and N_G MEGs, the probability of coverage of a typical load consumer randomly located within the power grid is as follows:

$$p_{cov,\ sys} = \frac{\overline{P_G}}{\overline{P_G} - \underline{P_G}} - \frac{(\overline{P_G} + \underline{P_G})(R_2^{2-\alpha} - R_{N_G}^{2-\alpha})T}{(\overline{P_G} - \underline{P_G})(\alpha - 2)\omega}\int_0^{+\infty}2\lambda_G^2\pi^2 r^{\alpha+1}e^{-\lambda_G\pi r^2}\mathrm{d}r$$

(34)

where $\overline{P_G}$ and $\underline{P_G}$ represent the upper and lower bounds, respectively, of the maximum output power of the MEGs; ω denotes the priority of the load consumer; $\alpha > 0$ is a weighting coefficient that measures the distance between the load consumer and the MEGs and the power consumed by the load consumer; T denotes the survivability threshold of the load consumer; R_2 and R_{NG} represent the distance from the load consumer to the second nearest MEG and the distance to the most distant MEG, respectively; and λ_G denotes the proportion of nodes deployed with MEGs in the power grid.

Proof The probability of coverage defined in Section III. D can be equivalent to the probability that a random load consumer achieves a target survivability threshold. A consumer is in coverage when its survivability is larger than threshold T, and it is dropped from the network for survivability below T. Conditional on the nearest MEG being at a distance r from the randomly chosen load consumer, the probability of coverage averaged over the entire grid is as follows:

$$
\begin{aligned}
p_{cov,sys} &= \mathbb{E}_r[\mathbb{P}(SI > T|r)] \\
&= \int_{r>0} \mathbb{P}(SI > T|r) f_{r_1}(r)\,\mathrm{d}r \\
&\stackrel{(a)}{=} \int_{r>0} \mathbb{P}\left(\frac{\omega \frac{P_G}{P_L} r^{-\alpha}}{\sum_{G_k \in \Phi/G_o} \frac{P_{G_k}}{P_L} r_k^{-\alpha}} > T \,\middle|\, r \right) 2\lambda_G \pi r e^{-\lambda_G \pi r^2}\,\mathrm{d}r
\end{aligned}
$$

(35)

where (a) follows from Campbell's theorem (Chiu et al., 2013) and (b) follows from (10) and (21).

The electrical energy produced by MEGs is practically generated by a controllable vehicle- mounted generator set, and the maximum output power of different MEG types falls within the range defined by the upper bound $\bar{P}_G$ and the lower bound $\underline{P}_G$. Therefore, the maximum output power of the MEG powering the chosen load consumer can be assumed to follow a uniform distribution $U \sim (\underline{P}_G, \bar{P}_G)$. Because the MEGs supplying power to this load consumer might differ under various failure scenarios, their maximum output power will also vary. Hence, we derive the probability of coverage accordingly:

$$
\begin{aligned}
\mathbb{P}\left(\frac{\omega \frac{P_G}{P_L} r^{-\alpha}}{\sum_{G_k \in \Phi/\{G_o\}} \frac{P_{G_k}}{P_L} r_k^{-\alpha}} > T \,\middle|\, r \right) &= \mathbb{P}\left(P_G > \frac{P_L T r^\alpha}{\omega} I_r \,\middle|\, r \right) \\
&\stackrel{(c)}{=} \mathbb{E}_{I_r}\left[\mathbb{P}\left(P_G > \frac{P_L T r^\alpha}{\omega} I_r \,\middle|\, r,\ I_r \right) \right] \\
&\stackrel{(d)}{=} \mathbb{E}_{I_r}\left(\frac{\overline{P_G} - \frac{P_L T r^\alpha I_r}{\omega}}{\overline{P_G} - \underline{P_G}} \,\middle|\, r \right) \\
&= \frac{\overline{P_G}}{\overline{P_G} - \underline{P_G}} - \frac{P_L T r^\alpha}{\omega(\overline{P_G} - \underline{P_G})} \mathbb{E}_{I_r}[I_r | r]
\end{aligned}
$$

(36)

where

$$
I_r = \sum_{G_k \in \Phi/\{G_o\}} \frac{P_{G_k}}{P_L} R_k^{-\alpha}
$$

(37)

Note that (c) follows from the properties of conditional expectations, and that (d) follows from the distribution function of the uniform distribution.

Applying Campbell's theorem (Chiu et al., 2013), the following expression for $\mathbb{E}_{I_r}[I_r | r]$ can be obtained:

$$
\begin{aligned}
\mathrm{E}_{I_r}\left[I_r | r \right] &= \mathrm{E}_{\Phi,\{P_{G_k}\}}\left[\sum_{G_k \in \Phi/\{G_o\}} \frac{P_{G_k}}{P_L} r_k^{-\alpha} \right] \\
&\stackrel{(e)}{=} \frac{1}{P_L} \mathrm{E}_\Phi\left[\mathrm{E}_{P_G}[P_G] \sum_{G_k \in \Phi/\{G_o\}} \frac{1}{r_k^\alpha} \right] \\
&= \frac{1}{P_L} \mathrm{E}_{P_G}[P_G] \mathrm{E}_\Phi\left[\sum_{G_k \in \Phi/\{G_o\}} \frac{1}{r_k^\alpha} \right] \\
&= \frac{\overline{P_G} + \underline{P_G}}{2 P_L} \mathrm{E}_\Phi\left[\sum_{G_k \in \Phi/\{G_o\}} \frac{1}{r_k^\alpha} I\left(R_2 \leq \|G_k\| \leq R_{N_G} \right) \right] \\
&= \frac{\overline{P_G} + \underline{P_G}}{2 P_L} \cdot \lambda_G \int_{R^2} \frac{1}{r^\alpha} I\left(R_2 \leq \|G_k\| \leq R_{N_G} \right) \mathrm{d}r \\
&= \frac{\overline{P_G} + \underline{P_G}}{2 P_L} \cdot \lambda_G \int_0^{+\infty} \int_0^{2\pi} \frac{1}{\rho^\alpha} I\left(R_2 \leq \|G_k\| \leq R_{N_G} \right) \mathrm{d}\theta \rho \,\mathrm{d}\rho \\
&= \frac{\overline{P_G} + \underline{P_G}}{2 P_L} \cdot 2\lambda_G \pi \int_{R_2}^{R_{N_G}} \frac{1}{\rho^\alpha} \rho \,\mathrm{d}\rho \\
&= \frac{\left(\overline{P_G} + \underline{P_G} \right) \lambda_G \pi}{(\alpha - 2) P_L} \cdot \left(R_2^{2-\alpha} - R_{N_G}^{2-\alpha} \right)
\end{aligned}
$$

(38)

where (e) follows from the independent identical distribution of P_G and its independence from point process Φ. Here, $\mathbb{I}(\cdot)$ denotes the indicator function.

By combining $(33) - (36)$, the expressions of the probability of coverage can be obtained:

$$
\begin{aligned}
p_{cov,sys} &= \int_0^{+\infty} \left[\frac{\overline{P_G}}{\overline{P_G} - \underline{P_G}} - \frac{(\overline{P_G} + \underline{P_G})\lambda_G \pi T r^\alpha}{(\overline{P_G} - \underline{P_G})(\alpha - 2)\omega} (R_2^{2-\alpha} - R_{N_G}^{2-\alpha}) \right] \cdot 2\lambda_G \pi r e^{-\lambda_G \pi r^2} \mathrm{d}r \\
&= \int_0^{+\infty} \frac{\overline{P_G}}{\overline{P_G} - \underline{P_G}} 2\lambda_G \pi r e^{-\lambda_G \pi r^2} \mathrm{d}r - \int_0^{+\infty} \frac{(\overline{P_G} + \underline{P_G})\lambda_G \pi T r^\alpha \left(R_2^{2-\alpha} - R_{N_G}^{2-\alpha} \right)}{(\overline{P_G} - \underline{P_G})(\alpha - 2)\omega} 2\lambda_G \pi r e^{-\lambda_G \pi r^2} \mathrm{d}r \\
&= \frac{\overline{P_G}}{\overline{P_G} - \underline{P_G}} - \frac{(\overline{P_G} + \underline{P_G})\left(R_2^{2-\alpha} - R_{N_G}^{2-\alpha} \right) T}{(\overline{P_G} - \underline{P_G})(\alpha - 2)\omega} \int_0^{+\infty} 2\lambda_G^2 \pi^2 r^{\alpha+1} e^{-\lambda_G \pi r^2} \mathrm{d}r
\end{aligned}
\tag{39}
$$

This completes the proof. $\square$.

Theorem 3 provides a general formulation for the coverage probability of load consumers in a power grid. It explicitly reveals and quantifies those factors that impact the coverage probability of load consumers, such as the number of deployed MEGs, the upper and lower bounds of the maximum output power of the MEGs, the power consumption of load consumers, the distance between load consumers and different MEGs, and the priorities and survivability thresholds of load consumers. This theorem describes the probability distribution of load consumers being covered by MEGs under different scenarios within a power network. Specifically, under varying scenarios, the power network structure varies, the distances between load consumers and MEGs change, and the maximum power output from the MEGs at different locations also changes. Consequently, the probability of load consumers being covered by MEGs varies across different scenarios. Therefore, to determine the coverage of load consumers by MEGs with different upper bounds of output power under different scenarios, Theorem 3 models the upper bound of the output power from any MEG as a random variable following a uniform distribution. To characterize the variation in distance between load consumers and MEGs across different scenarios, the concept of conditional expectation is employed to calculate the conditional probability distribution of the coverage probability of load consumers given a specific distance distribution.

Corollary 4. In a power grid with N_L load consumers and N_G MEGs, the load shedding within the power grid can be expressed as follows:

$$
LS_{sys} = \left(1 - \frac{\overline{P_G}}{\overline{P_G} - \underline{P_G}} - \frac{(\overline{P_G} + \underline{P_G})(R_2^{2-\alpha} - R_{N_G}^{2-\alpha})T}{(\overline{P_G} - \underline{P_G})(\alpha - 2)\omega} \int_0^{+\infty} 2\lambda_G^2 \pi^2 r^{\alpha+1} e^{-\lambda_G \pi r^2} \mathrm{d}r \right) \sum_{i \in N_L} P_{L_i}
\tag{40}
$$

Proof The relationship between the coverage probability and the load shedding of a power grid is as follows:

$$
LS_{sys} = (1 - p_{cov,\,sys}) \sum_{i \in N_L} P_{L_i}
\tag{41}
$$

By substituting (41) into (34), we derive Corollary 4.

This completes the proof. $\square$.

Theorem 3 provides valuable insights for improving the structural resilience of a power grid, including increasing the number and output of MEGs, and optimizing the distance distribution through deploying MEGs and adding parallel lines, which could serve as useful reference for decision-makers. Such insights also shed light on the explicit impact of power grid structures, MEG deployment decisions, and external extreme weather events on power grid resilience. Corollary 4 provides the information necessary to quantify the factors affecting load shedding, and it offers valuable insights for reducing load shedding within a power grid.

In summary, (34)-(41) establish the relationship between the structural features (distance distribution) and the structural resilience (coverage probability, load shedding) of a power grid, as well as MEG deployment decisions. The analytical results provide valuable information for evaluating the impact of structural features and MEG deployment decisions on the structural resilience of a power grid.

4. Case study

In this section, we conduct case studies on a 33-bus distribution system (Baran and Wu, 1989) and on a 118-bus distribution system (Zhang et al., 2007) to verify the effectiveness of the proposed method. The cases were tested in MATLAB 2019a on a personal computer with a 3.00 GHz i5 processor and 16 GB RAM.

4.1. 33-bus distribution system

This system consists of 33 buses, 32 lines, and 5 tie lines, with a voltage of 12.66 kV, and load size of 3.715 MW, and 2.3 MVar.

1) *Effectiveness of the distance measure:* In the context of electric power grids, the electrical distance is used widely to quantify the electrical connection between any two nodes in many power system problems (Lagonotte et al., 1989)– (Poudel et al., 2018). We perform comparative analysis of computational outcomes utilizing the electrical distance and the proposed distance measure to validate the soundness and effectiveness of the proposed distance measure. Specifically, we focus on evaluating the capability of

electrical distance and the proposed distance measure to accurately reflect fluctuations in electrical connections between power grid nodes during fault conditions. It should be noted that in the case study, we consider only line faults under the impact of extreme weather events.

We consider a single-line fault scenario where the power line connecting node 10 and node 11 experiences failure; the location of the failed line can be seen in Fig. 1(a). Comparison of the distribution of distances between node 10 and node 11 under normal and failure conditions is presented in Fig. 5. It should be noted that nodes 10 and node 11 are associated with the failed line. The changes in the electrical connections of node 10 and 11 with the other nodes in the power grid reflect the direct impact of line faults on associated nodes. Fig. 5(a) and Fig. 5(b) show the changes in the distance measure between node 10 and node 11 with the remaining nodes in the power grid before and after the line failure; Fig. 5(c) and Fig. 5(d) illustrate the changes in electrical distances between node 10 and node 11 with the other nodes. From Fig. 5(a) and Fig. 5(b), it is apparent that, compared with the normal condition, the line failure leads to increase in the distance measure between node 10 and node 11 and the other nodes, thereby indicating weakening in their electrical connections. Notably, there is marked increase in the distance between node 10 and nodes 11–18, as well as between node 11 and nodes 1–9, signifying notable reduction in their electrical connections. Intuitively, the failure of line 10–11 severs the direct connection path linking node 10 to nodes 11–18, as well that linking node 11 to nodes 1–9. Consequently, those nodes can rely only on tie lines for connectivity, thereby resulting in deterioration of their electrical connections. The results presented in Fig. 5(a) and Fig. 5(b) align harmoniously with this intuitive understanding.

Fig. 5(c) and Fig. 5(d) reveal that the line failure causes escalation in the electrical distance between node 10 and node 11 with respect to the other nodes, compared with the normal condition. As per the designated definition of electrical distance (Lagonotte et al., 1989)– (Poudel et al., 2018), this increase signifies rise in the mutual impedance between node 10 and node 11, impacting their current transmission capacity and subsequently leading to weakening of their electrical connection. Additionally, it is worth mentioning that the electrical distance between node 10 and itself, and electrical distance between node 11 and itself experience substantial rise following the line fault, indicating marked increase in their self-impedance. This reflects the impact of the line failure on the associated nodes.

By analyzing Fig. 5(a)-Fig. 5(d), we can deduce that both the proposed distance measure and the electrical distance possess the capability to support quantification of the impact of line failure on the electrical connections between the nodes associated with the failed line and other nodes in the power grid. In comparison to electrical distance, the proposed distance measure can better quantify the changes in electrical connections between the associated nodes and the other nodes, which are inherently influenced by the topological structure of the power grid. This discrepancy is particularly evident when recognizing that the change in distance between node 11 and nodes 1–9, surpass that of other nodes owing to the disruption of their direct connection pathway.

Fig. 6(a) and Fig. 6(b) illustrate the changes in the distance measure and the electrical distance from node 1 to the remaining nodes before and after the occurrence of the fault, respectively. It is evident that the occurrence of the line fault leads to increase in both the distance measure and the electrical distance between node 1 and the other nodes, indicating deterioration in their electrical interconnections. Although direct impact of the line 10–11 fault on the lines associated with node 1 is absent, its influence remains evident owing to the disruption of the direct path connecting node 1 and nodes 11–18, thereby weakening their electrical connections. Notably, the extent of this deterioration in terms of the electrical connections between node 1 and nodes 11–18 can be quantified by utilizing both the distance measure and the electrical distance, aligning with our intuitive expectations. Moreover, in comparison to the electrical distance, the distance measure possesses superior ability to accurately differentiate nodes experiencing notable changes in electrical connections.

In the second fault scenario, both line 10–11 and line 2–19 are considered affected by extreme weather events, as depicted in Fig. 1(a). Note that in the multiple-line fault scenarios considered in this paper, cascading failures are considered. Fig. 7 illustrates the distance distributions of node 2 and node 5 under three scenarios: normal conditions, fault on line 10–11, and faults on line 10–11 and line 2–19.

Specifically, Fig. 7(a) and Fig. 7(b) illustrate the distance measure distributions for node 2 and node 5, respectively, under the three scenarios. Fig. 7(c) and Fig. 7(d) represent the electrical distance distributions for node 2 and node 5, respectively. When only line 10–11 fails, node 2 is not associated with the failed line. Therefore, its response to the line failure is primarily reflected in increase in the distance measure and weakening of the electrical connections between node 2 and nodes 11–18. However, when line 2–19 also fails, node 2 is affected directly. The distance measure between node 2 and nodes 11–18 further increases, and there is a notable increase in the distance to nodes 19–22, indicating substantial weakening of the electrical connections, as depicted in Fig. 7(a). Regarding electrical distance, Fig. 7(c) shows that the electrical distance from node 2 to the other nodes increases after the fault occurs on line 10–11, and it increases further after the fault occurs on line 2–19. It is worth noting that the notable increase in electrical distance between node 2 and nodes 11–22 after the line faults reflects the impact of the line failure on the electrical connections between them. Intuitively, when line 10–11 fails, the direct connection path between node 2 and nodes 11–18 is disrupted, and they can only be connected through tie lines, resulting in weakening of their electrical connections. When line 2–19 also stops operating, the direct connection path between node 2 and branch 19–22 is interrupted, causing substantial weakening of the electrical connections. Furthermore, the path connecting node 2 and nodes 11–18, comprising line 2–19, branch 19–22, and tie line 22–12, is interrupted, leading to further weakening of the electrical connections between them. The changes in electrical connections shown in Fig. 7(a) and Fig. 7(c) align with this intuitive analysis.

After the faults on both line 10–11 and line 2–19, node 5 is not associated with the failed lines. Fig. 7 demonstrates that even though node 5 is not located at the ends of the failed lines, its distance measure to nodes 11–18 and nodes 19–22 increases after the faults occur. Moreover, it can be observed that the distance measure from node 5 to nodes 19–22 increases more noticeably after the
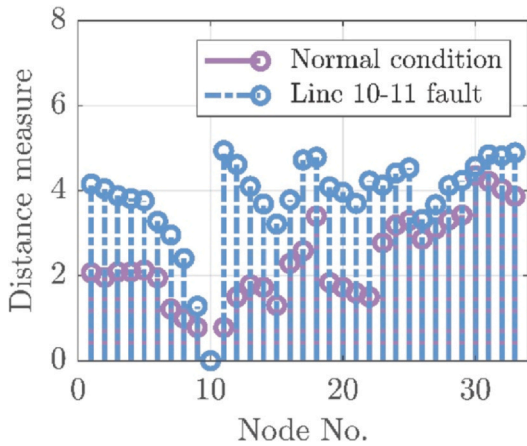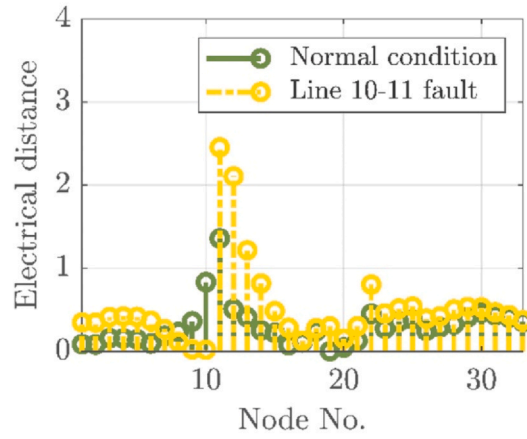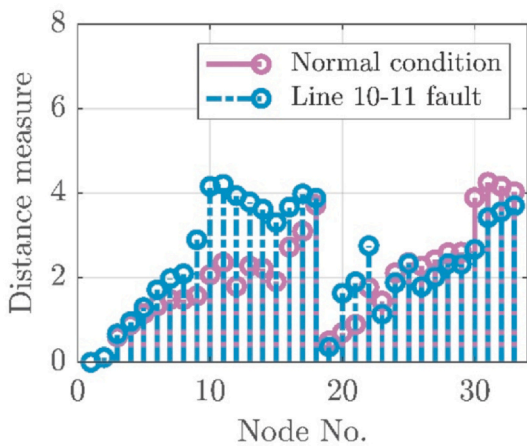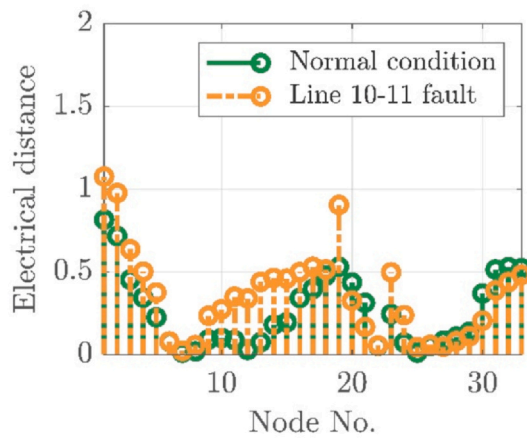
(a) Node 10
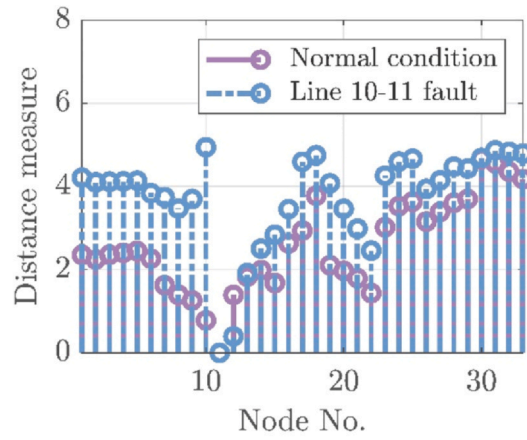
(b) Node 11
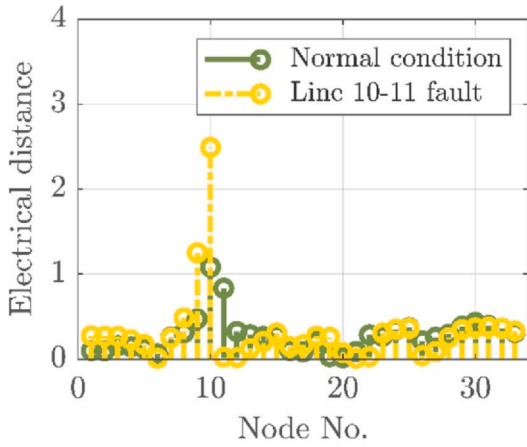
(c) Node 10

(d) Node 11

Fig. 5. Distance distribution of nodes 10 and 11 under normal and fault conditions.

(a) Distance measure

(b) Electrical distance

Fig. 6. Distance distribution of node 1 under normal and fault conditions.
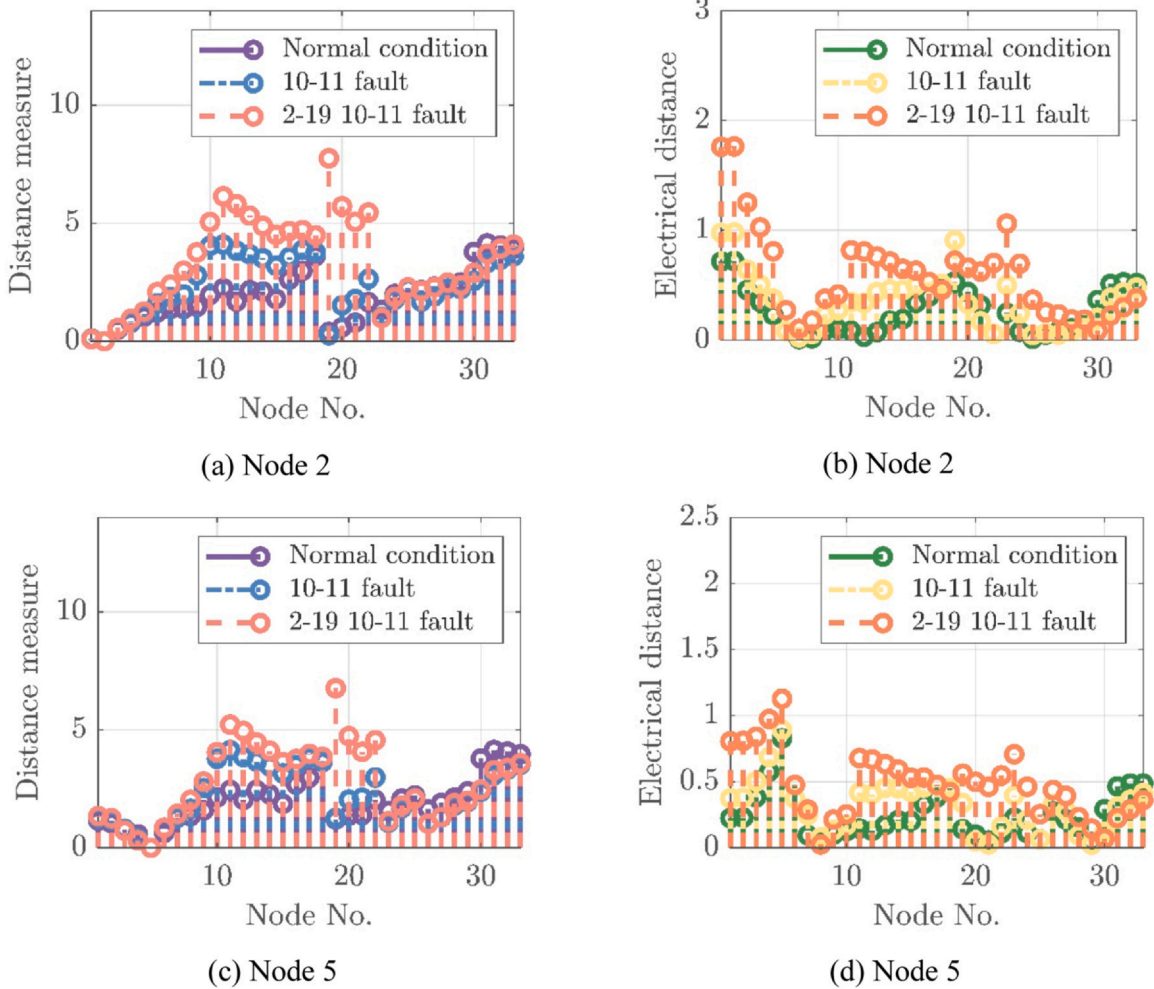
(a) Node 2

(b) Node 2

(c) Node 5

(d) Node 5

Fig. 7. Distance distribution of nodes 2 and 5 under normal and fault conditions.

fault on line 2–19, whereas the increase in the distance measure from node 5 to nodes 11–18 mainly occurs after the fault occurs on line 10–11. Consideration of the electrical distance distribution for node 5 shown in Fig. 7(d) reveals that the increments occur primarily for nodes 11–18 and nodes 19–22. Intuitively, the disconnection of line 10–11 and line 2–19 removes the direct connection paths between node 5 and nodes 11–18 and nodes 19–22. The results shown in Fig. 7(b) and Fig. 7(d) reflect the changes in the electrical connections and align with our intuitive analysis. It is worth mentioning that, compared with electrical distance, the distance measure of the relevant nodes shows more notable increase after the corresponding line faults, providing better discrimination, maintaining accuracy, and offering better characterization of the changes in electrical connections between power grid nodes.

Figs. 5–7 display the variations in electrical connections between the nodes located at the ends of the failed lines and the nodes at other locations before and after a failure scenario. Next, we consider all scenarios for a certain type of line failure, including scenarios with one-line faults, scenarios with two-line faults, and scenarios with three-line faults. We analyze the average changes in the electrical connections between nodes under all scenarios for a given type of line failure, as shown in Fig. 8.

Fig. 8(a) and Fig. 8(b) show the distribution of the average distance measure and the distribution of the average electrical distance, respectvely, from each node in the power grid to other nodes under normal conditions and under the three failure scenarios. Note that in the 33-node distribution system, we account for the states of 37 lines, including 32 branches and 5 tie lines. Therefore, there are 37 scenarios with a single-line fault, 666 scenarios with a two-line fault, and 7770 scenarios with a three-line fault in the power grid. We consider all scenarios of the three differentline failure types, and compute the average distance measure and the average electrical distance for each node across all scenarios.

From Fig. 8(a), it can be observed that compared with the findings in the failure scenarios, each node exhibits the smallest average distance measure to the other nodes under normal conditions, indicating stronger electrical connection. Following the occurrence of the line faults, the average distance measure from each node to the other nodes increases as the number of failed lines grows, suggesting weakening of the electrical connections between nodes. Additionally, it is noteworthy that the average distance measure
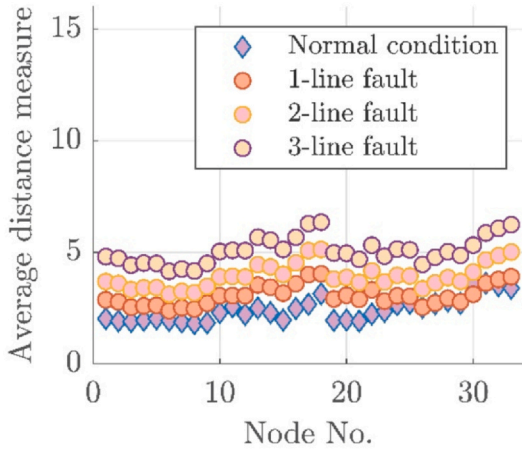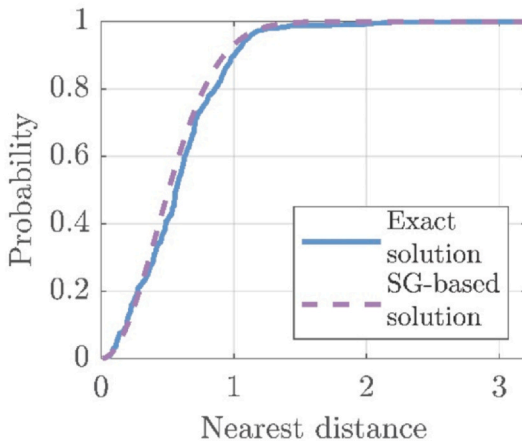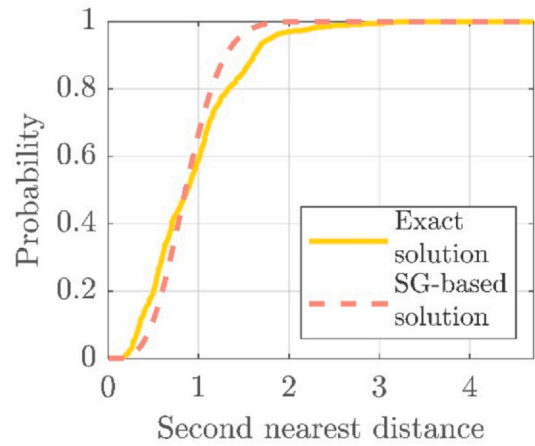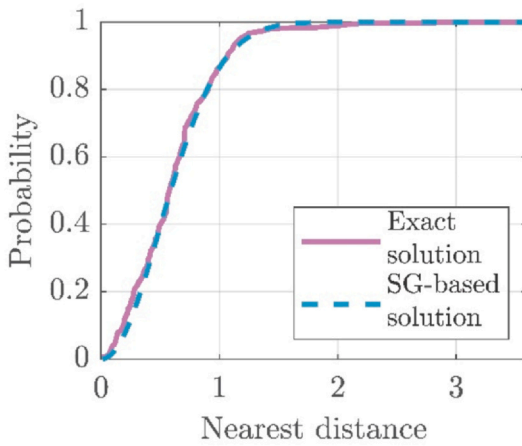
(a) Distance measure
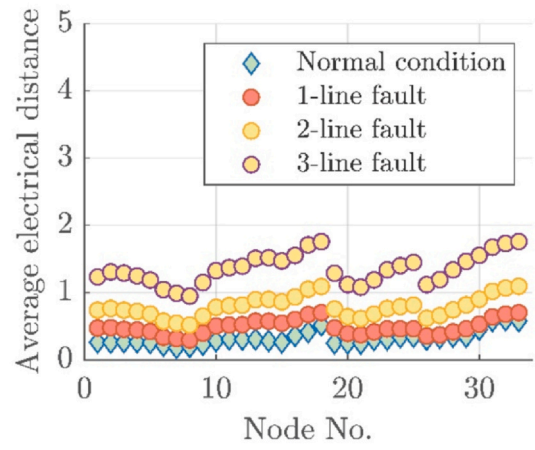
(b) Electrical distance

Fig. 8. Node average distance distribution under different conditions.
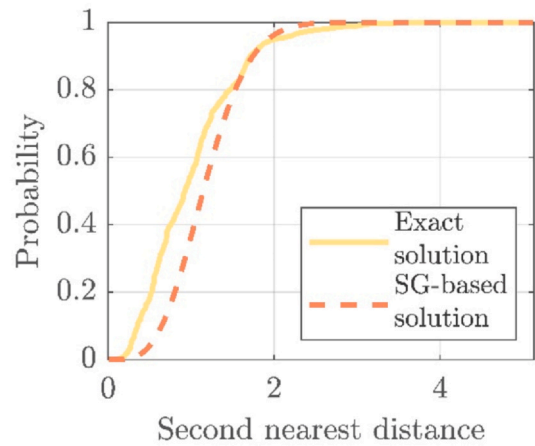

(a) 2-line fault

(b) 2-line fault

(c) 3-line fault

(d) 3-line fault

Fig. 9. Probability distribution function of distance measure under line fault conditions.

Table 1
Node distance expectation.

Distance	Normal		1-line fault		2-line fault		3-line fault	
	Exact	SG	Exact	SG	Exact	SG	Exact	SG
Nearest	0.5609	0.5000	0.5627	0.5069	0.5895	0.5414	0.6161	0.6263
2nd nearest	0.8581	0.7500	0.8704	0.7603	0.9392	0.8121	1.0088	0.9395
3rd nearest	1.1921	0.9375	1.2181	0.9504	1.3345	1.0152	1.4622	1.1743
4th nearest	1.3987	1.0938	1.4928	1.1088	1.6574	1.1844	1.8408	1.3701

exhibits a similar distribution pattern across all four scenarios. Specifically, for nodes 9–15, the average distance measure in all four scenarios shows an initial increase followed by reduction, implying that their electrical connections with other nodes transition from weak to strong and then weaken again, aligning with the topology of the grid. Both node 9 and node 15 are connected to tie lines, thereby enhancing their electrical connections with other nodes under both normal and failure scenarios. Moreover, node 12 can establish connections with other branches through tie line 12–22, resulting in a slightly smaller distance measure compared with that of node 10 and node 13.

Conversely, the average distance measure of node 16, node 17, and node 18 increases sequentially, corresponding to their respective locations within the power grid. Node 18, at the end of branch 1–18, faces relatively greater challenges in maintaining connections with the other nodes during the line faults. The difference in the average distance measures between node 19 and node 18 also indicates that they do not belong to the same branch, with node 19 exhibiting stronger electrical connections with other nodes in accordance with the power grid topology. For nodes 26–33, their average distance measures demonstrate an overall trend of increase across all four scenarios. However, node 29 displays a slightly smaller average distance measure compared with the other nodes on the same branch. According to the grid structure, we can deduce that node 29 is connected to node 25 through tie line 29–25, which reinforces its electrical connections with the other nodes.

Based on the above analysis, it is evident that the calculated results derived from the proposed distance measure reflect the influence both of the number of failed lines and of the power grid structure on the electrical connections between nodes. The results presented in Fig. 8(b) further validate the aforementioned analysis. It can be observed that as the number of line faults increases, the average electrical distance from each node to another also increases, displaying similar distribution patterns across different types of line faults. From node 1 to node 18, the average electrical distance initially declines and then increases. Considering the power grid structure, nodes located at the ends of branches need to traverse more branches to establish electrical connections with other nodes in the network, thereby resulting in higher mutual impedances compared with those of nodes closer to the center of the branches. This corresponds to the larger electrical distances depicted in Fig. 8(b). For nodes 19–25 and nodes 26–33, their average electrical distance distributions indicate that they do not belong to the same branch, reflecting the influence of the power network structure on the electrical connections between nodes.

In summary, the results shown in Figs. 5–8 indicate that the proposed distance measure, in contrast to the electrical distance, has the capability to more accurately quantify the changes in electrical connections between nodes associated with failed lines and nodes associated with normal lines under fault conditions. Moreover, the average node distance measure in the line failure scenarios can effectively capture the impact both of the number of failed lines and of the network structure on the electrical connections among nodes.

2) *Numerical characteristics of distance measure:* Based on the quantification of node distances using the distance measure, we compute the precise numerical characteristics of node distances and compare them with theoretical outcomes to validate the effectiveness of the theoretical expressions.

Theorem 2 presents the distribution function of distances between any node in the network and its neighboring nodes at varying distances. We compare the actual distribution of node distances obtained by analyzing all line fault scenarios with the computed results derived from Theorem 2, as shown in Fig. 9. Fig. 9(a) exhibits the real distribution of distances from each node to its nearest neighbor node, together with the corresponding theoretical distribution based on SG when two lines fail within the power network. Fig. 9(b) displays the actual distribution of distances from each node to its second-nearest neighbor node, accompanied by the theoretical distribution. Note that we traverse a total of 666 scenarios where two lines fail and calculate the distances between each node to its nearest and second-nearest neighboring nodes. Furthermore, when the power network experiences the three-line faults, we traverse all 7770 scenarios and calculate the distances between each node and its nearest and second-nearest neighboring nodes. The comparison results between the actual distribution of distances and the theoretical results are shown in Fig. 9(c) and Fig. 9(d). Notably, the theoretical expression of the node distance distribution provided by Theorem 2 closely approximates the actual distribution, as observable in Fig. 9(a)-Fig. 9(d).

Propositions 2 and 3 offer the expectation of distance and the second origin moment of distance from any node to its neighboring nodes in the event of structural changes in the power grid. To validate Proposition 2, we calculate the average distances between nodes and their neighboring nodes under both normal and various fault conditions. We compare the calculated results with the results obtained from Proposition 2, as shown in Table 1.

From Table 1, it can be observed that as the number of failed lines increases, Proposition 2 quantifies the growth in the expectation of distance between any node and its neighboring nodes within the network. Under both normal conditions and fault

Table 2
Node distance second origin moment.

Distance	Normal		1-line fault		2-line fault	
	Exact	SG	Exact	SG	Exact	SG
2nd nearest	0.8862	0.6079	0.9555	0.6422	1.1484	0.8358
3rd nearest	1.6624	1.2159	1.7202	1.2843	2.1425	1.6716
4th nearest	2.2847	2.0264	2.5252	2.1406	3.2362	2.7860

conditions, Proposition 2 enables quantification of the distribution of average distances between nodes and their neighboring nodes. Through comparison of the theoretical results provided by Proposition 2, presented in the "SG" column, to the actual expected distances between nodes, listed under the "Exact" column, we observe close approximation between the theoretical values and the computed values, with errors falling within an acceptable range.

To substantiate Proposition 3, we compute the second origin moment of distances between nodes and their neighboring nodes, considering both normal and various fault conditions. The calculated results are compared with the results obtained from Proposition 3, as shown in Table 2.

As depicted in Table 2, noticeable correlation emerges between the escalation in line faults and the increase of the second origin moment of distances between nodes. This indicates greater dispersion in distance values, highlighting more distinct electrical connections between different nodes. Furthermore, within a given scenario, the dispersion of distance values is greater with nodes at greater distances. The theoretical results based on SG effectively capture the changing trend of the second origin moment of distances between nodes and provide relatively conservative results compared with actual outcomes.

3) *Coverage probability and load shedding:* To validate our proposed resilience metrics of coverage probability and load shedding, we compare the results obtained from the SG-based theoretical framework, i.e., Theorem 3 and Corollary 4, to the optimization outcomes based on the maximum covering model (Mak and Shen, 2016). The maximum covering problem is used widely to tackle the classical operational optimization problem of facility location. We utilize the maximum covering model to determine the pre-positioning strategy for MEGs before the occurrence of extreme events. The underlying optimization principle of this approach lies in selecting locations for MEG deployment that maximize the total load that can be restored under the constraint of the total number of MEGs. For comparative experiments, we consider all 666 scenarios where two lines in the power grid fail. Under various scenarios, the power output limit of the MEG is uniformly distributed within the range of 500 kW and 800 kW. The computed values of the coverage probability and load-shedding metrics based on the two methods are illustrated in Fig. 10.

Fig. 10 (a) exhibits the trend of the coverage probability metric as the number of MEGs varies. When two lines fail in the 33-bus distribution system, deploying six MEGs achieves an average coverage of 55% of the load under all potential failure scenarios, whereas deploying eight MEGs covers an average of 90% of the load. Fig. 10 (b) illustrates the declining trend of load shedding in the power grid as the number of MEGs increases, eventually reaching zero. However, as the number of deployed MEGs exceeds nine, the marginal benefit gained by reducing load shedding attributable to further deployment diminishes substantially. Both Fig. 10 (a) and
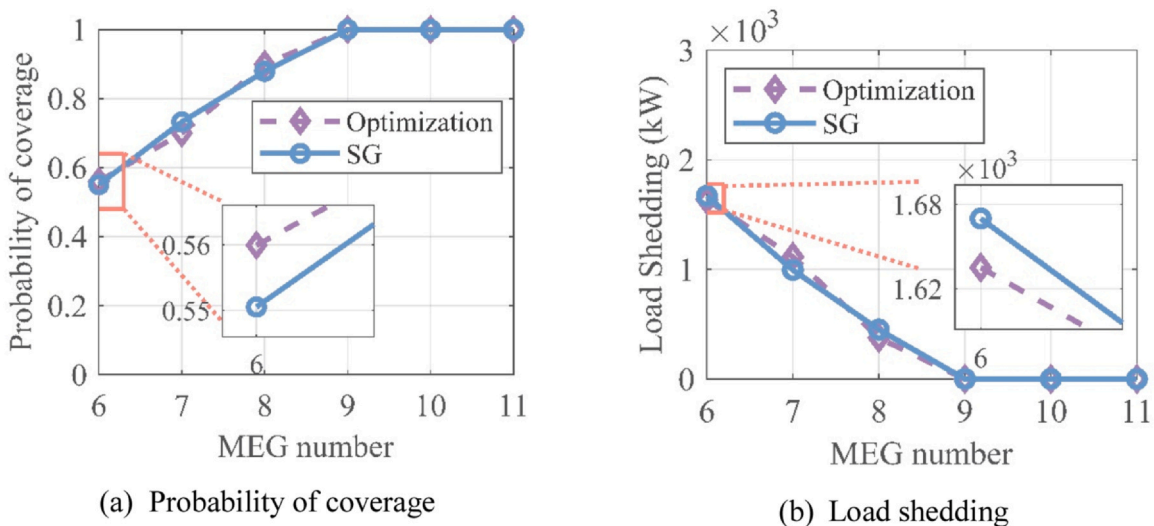

(a) Probability of coverage

(b) Load shedding

Fig. 10. Resilience metrics of the 33-bus distribution system.

(a) Probability of coverage   (b) Load shedding
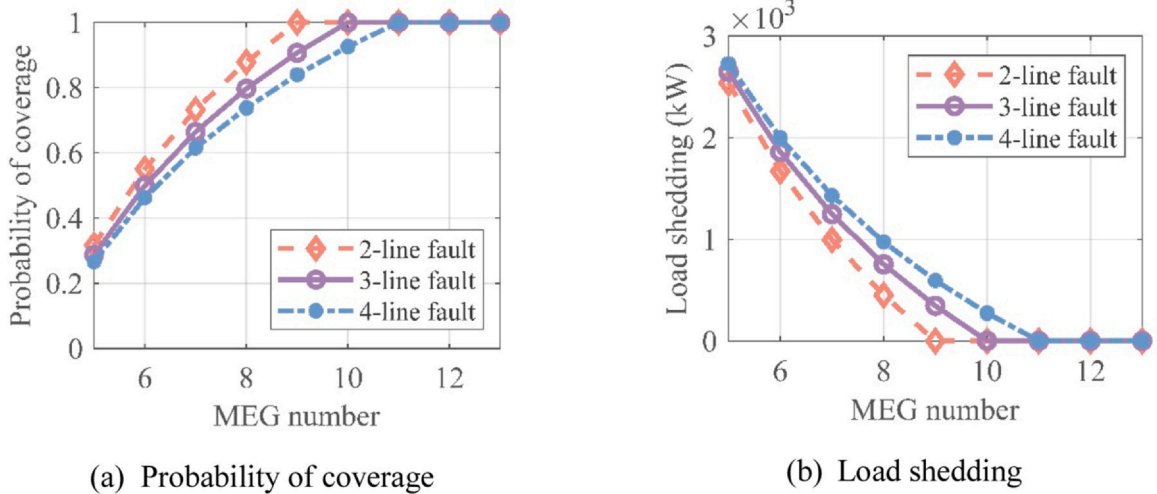
Fig. 11. Resilience metrics of 33-bus distribution system based on SG when multiple lines fail.

Table 3
Comparison of the Operation time on the 33-bus system.

Fault	Time/h		Number of scenarios
	SG	Optimization	
2-line fault	370.15	3383.88	666
3-line fault	4318.45	-	7770
4-line fault	36706.86	-	66045

Fig. 10 (b) demonstrate that the results obtained from the SG-based theoretical approach closely align with the optimization outcomes based on the maximum covering model. This suggests that the SG-based theoretical approach proposed here can serve as an approximate method for assessing the impact of MEG quantity on the ability to cover the load, thereby offering valuable insights regarding power grid operation.

Fig. 11 illustrates the variations in coverage probability and load shedding metrics, computed using SG. It is apparent that for a fixed number of MEGs, an increase in the number of line faults results in reduced load coverage and increased load shedding. To achieve the desired coverage objectives and to mitigate economic losses caused by load shedding, additional MEGs must be deployed.
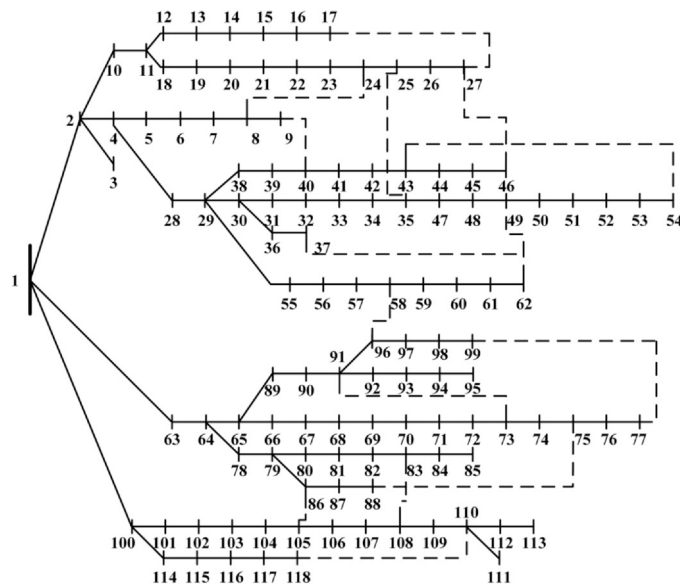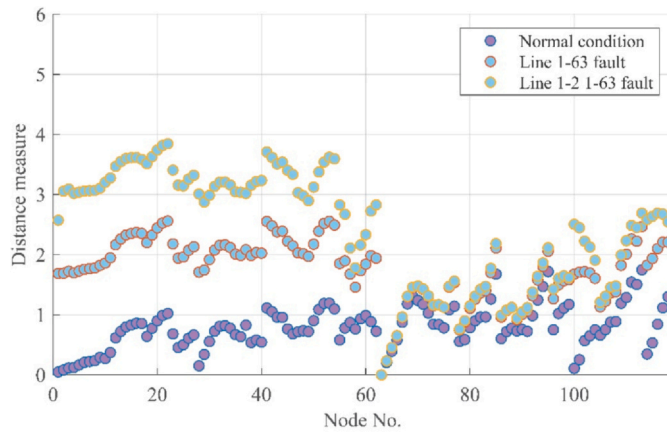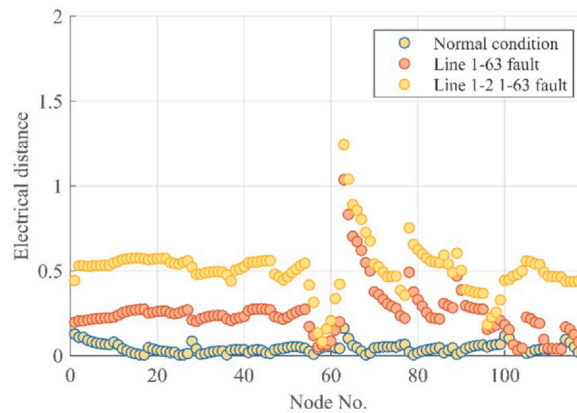

Fig. 12. Initial configuration of the 118-bus test system.

(a) Distance measure

(b) Electrical distance

Fig. 13. Distance distribution of node 63 under three different conditions.

Fig. 11 provides clear depiction of the interrelationship between MEG quantity and grid resilience, considering all possible scenarios of multiple line failures. This offers valuable guidance to system operators when making MEG deployment decisions.

4) *Running time comparison:* Comparison of the operation time between these two methods is presented in Table 3. It is apparent that our proposed SG-based approach exhibits notable superiority in terms of running time compared with the optimization method. As the number of failed lines increases, the number of fault scenarios rises markedly. Employing optimization techniques imposes substantial computational expense, and the symbol "-" within the table denotes inability to compute the results. The proposed SG-based method provides strong support for rapid and effective assessment of how the quantity of MEGs deployed impacts grid resilience and load survivability under different failure scenarios.

4.2. 118-bus distribution system

This system is a 11 kV distribution system with 118 buses, 117 sectionalizing switches, and 15 tie switches, as shown in Fig. 12. Detailed data can be found in (Zhang et al., 2007).

1) *Effectiveness of the distance measure:* Results of assessment of the effectiveness of the distance measure and of the electrical distance in characterizing the electrical connection among nodes within a 118-node distribution system are presented in Fig. 13 and Fig. 14.

Fig. 13 and Fig. 14 present the distance distributions of node 63 and node 20 under three scenarios: normal conditions, fault on line 1–63, and fauts on line 1–2 and line 1–63. Fig. 13 (a) displays the distance measure of node 63 from which we make. We have the following observations. (i) Compared with that under normal conditions, the distance measure between node 63 and the other nodes increases under both fault scenarios. (ii) The distance measure between node 63 and nodes 1–62 increases substantially after the fault on line 1–63, and increases further after the fault on line 1–2. An explanation is that the connectivity path connecting node 63 and the component consists of nodes 2–62 and involves four main lines: line 1–2, line 1–63, line 1–100, and tie line 96–58. When line 1–63.
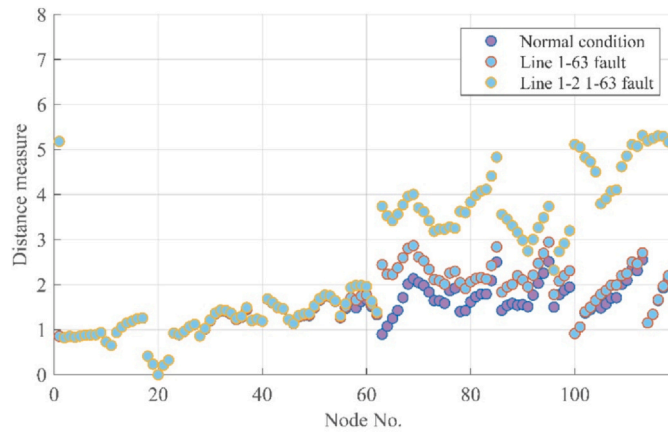
(a) Distance measure
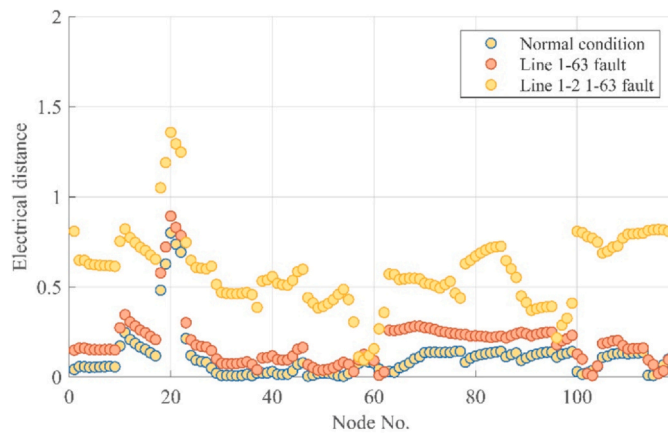
(b) Electrical distance

Fig. 14. Distance distribution of node 20 under three different conditions.

fails, the direct connectivity path between node 63 and nodes 2–62 is disrupted, thereby weakening their electrical connection. Furthermore, when line 1–2 also fails, node 63 can only establish connection with nodes 2–62 through tie line 96–58, leading to further attenuation of the electrical connection. However, these line faults do not occur within the component formed by nodes 64–118, consequently, it causes only minor impact on the electrical connection between node 63 and nodes 64–118. The computed distance measure effectively quantifies the impact on node 63 of faults on line 1–63 and line 1–2. As shown in Fig. 13 (b), it is evident that the electrical distance between node 63 and the other nodes increases substantially after the fault on line 1–63, and increases further when faults occur on both line 1–2 and line 1–63, thereby confirming the conclusions derived from the distance measure presented in Fig. 13 (a).

Fig. 14 (a) and Fig. 14 (b) present the distribution of the distance measure and of the electrical distance from node 20 to the other nodes under three different scenarios. In those failure scenarios, node 20 is not associated with the failed lines, but its electrical connections with the other nodes are still affected by line faults. It can be observed in Fig. 14 (a) that line faults have negligible impact on the distance measure between node 20 and both nodes 1–19 and nodes 21–62. This is attributable to the fact that the faults on lines 1–2 and 1–63 have no impact on the internal structure of the connected component comprising nodes 2–62. The primary connectivity path between node 20 and the nodes residing in that connected component remained unchanged. Hence, the variations in electrical connections between node 20 and nodes 2–62, as quantified by the distance measure, are not substantial. The notable increase in the distance measure between node 20 and nodes 63–118 signifies the impact of line faults on node 20. The line faults destroy the direct path between node 20 and the connected component containing nodes 63–118. Consequently, node 20 can only establish connections with nodes 63–118 via tie line 96–58, which weakens the connection between them considerably. In Fig. 14 (b), it is evident that line faults induce an increase in the electrical distance between node 20 and the other nodes, especially after line 1–2 fails. When only line 1–63 is destroyed, node 20 still maintains its electrical connections with the connected component comprising nodes 63–118 through lines 1–2 and 1–100. The impact of the line 1–2 failure on node 20 is greater because electrical connections with nodes 63–118 can only be established through tie line 96–58 rather than through lines 1–2 and 1–100. Consequently, the electrical distance increases substantially, aligning with the conclusions drawn from Fig. 14 (a). Fig. 13 and Fig. 14 depict the effects
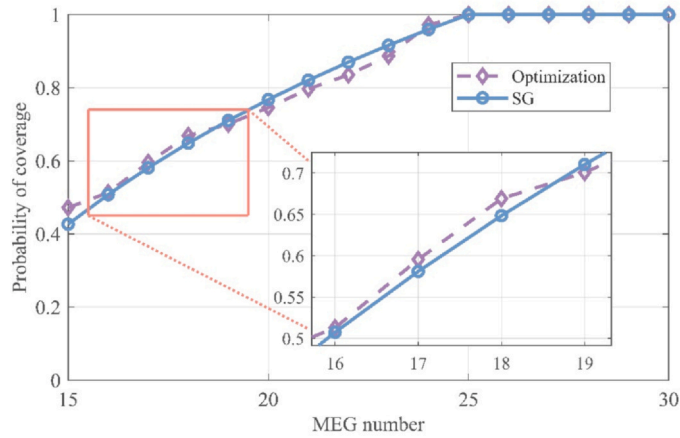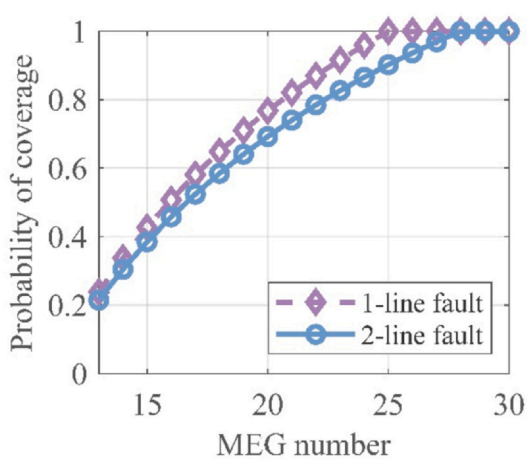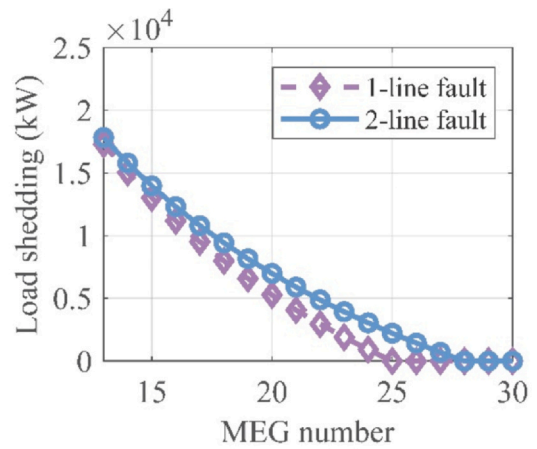
(a) Probability of coverage
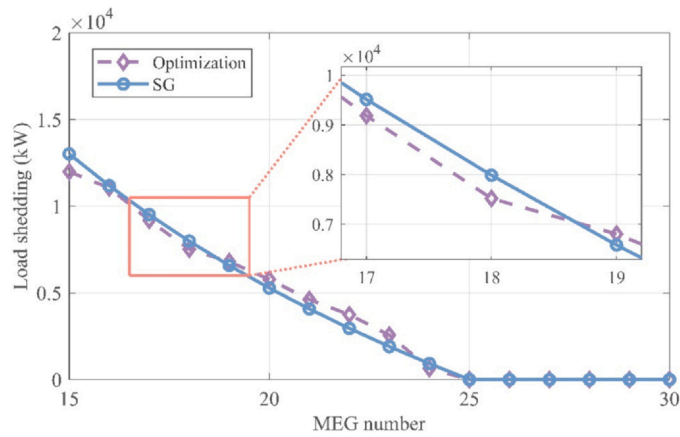
(b) Load shedding

Fig. 15. Resilience metrics of the 118-bus distribution system.

(a) Probability of coverage

(b) Load shedding

Fig. 16. Resilience metrics of 118-bus distribution system.

71

Table 4
Comparison of the Operation time on the 118-bus system.

Fault	Time/h		Number of scenarios
	SG	Optimization	
1-line fault	1.10	17.57	132
2-line fault	71.92	-	8646

of line faults on nodes both associated and unassociated with the failed lines, highlighting how the distance measure effectively captures the impact of line faults on the electrical connections between power grid nodes, considering the inherent structure of the network.

2) *Coverage probability and load shedding:* When one line fails in the 118-bus power grid, the total number of scenarios is 132, including scenarios with tie line faults. Across different scenarios, the upper limit of power output from the MEG is uniformly distributed between 500 and 800 kW. We compare the theoretical outcomes based on SG with the optimization results based on the maximum covering model, as depicted in Fig. 15. Fig. 15 (a) and Fig. 15 (b) illustrate the variations in coverage probability and load shedding metrics of the power grid, respectively, as the quantity of deployed MEGs varies. The proposed SG-based method yields computational results that are consistent with the optimization outcomes. It effectively quantifies the performance pertaining to the coverage probability and the load survivability under different quantities of MEGs. Moreover, it demonstrates the marginal effects of increasing the number of MEGs. For example, when the number of MEGs increases from 15 to 19, the coverage probability rises from 47% to 70%. However, as the number of MEGs continues to increase to 23, the coverage probability only increases from 70% to 88%. This marginal effect is also demonstrated in the above case study of the 33-bus power grid.

Fig. 16 shows the variations in coverage probability and load shedding metrics of the 118-bus distribution system obtained from the SG-based method. All scenarios of 1-line faults and 2-line faults are considered. Fig. 16 effectively portrays the expected coverage probability and load shedding given a fixed number of MEGs, which serves as invaluable guidance for system operators when formulating deployment strategies.

3) *Running time comparison:* Table 4 illustrates comparative analysis of the running time of those two approaches in the 118-bus distribution system. Obviously, the proposed method reduces the computational time substantially, thereby facilitating rapid evaluation of MEG deployment strategies in practice. Furthermore, compared with that with the above 33-bus power network, the computational time based on the optimization method experiences rapid escalation as the network size increases to 118 buses, and the computational cost for the scenario of 2-line faults is extremely high. However, our proposed approach displays noticeably greater reduction in computation time, showcasing its exceptional capability in handling large-scale networks and vast scenarios.

4) *Discussion:* As another representative of mobile power sources, the application prospects of mobile energy storage systems (MESSs) in the SG-based framework proposed in this paper are clear. Specifically, similar to MEGs, MESSs (Wang et al., 2022)– (Sadegh et al., 2022) can also supply emergency power to critical loads, thereby enhancing power system resilience against extreme events through pre-deployment. Within the SG-based framework presented in this paper, the spatial distribution of MESSs and critical loads in the grid can be effectively modeled using point processes. Through the computation of the distances between them based on the distance measure, coupled with the utilization of Voronoi tessellation, the service coverage of each MESS can be determined. The derivation processes of the proposed resilience assessment metrics and the theoretical expressions remain applicable by simply replacing the parameters of the MEGs with those of the MESSs. Consequently, the SG-based framework for power system resilience assessment, as proposed in this paper, can be readily extended to incorporate MESSs.

5. Conclusion

This paper proposes a novel SG-based method to address structure uncertainty in distribution networks induced by extreme weather events, and to evaluate the performance of MEG pre-positioning decisions. The point process approach is adopted to describe potential location distributions of power grid components across diverse scenarios. The proposed distance measure effectively captures the changes in electrical connections between power grid components before and after failures occur. The closed-form expressions of the distance distribution between power grid elements, based on Poisson point processes, closely approximates the actual distance distribution. Subsequently, Voronoi tessellation is utilized to illustrate the coverage of different MEGs for load consumers. Finally, effective resilience assessment metrics are defined, and the analytical expressions of those metrics are derived and demonstrated, explicitly revealing the impact of power grid structural characteristics and MEG deployment decisions on grid resilience during the occurrence of extreme events. The following conclusions are derived based on analysis of case studies.

1) The proposed distance measure successfully captures changes in electrical connections between power grid components under various line failure scenarios. Compared with the electrical distance, the proposed distance measure more effectively reflects the weakening of electrical connections between components associated with failed lines and other components.

2) The closed-form expressions of distribution functions and expectations of the proposed distance measure adequately describe the numerical characteristics of the distances between power grid components across diverse scenarios, thereby characterizing structure uncertainty induced by extreme events. As the number of failed lines increases, the distance between each component in the power grid and its neighboring components increases. This results in rightward shift of the distance distribution curve and increase in the expectation of distances between all components.

3) The proposed resilience metrics and their corresponding analytical expressions explicitly reveal the influence of MEG deployment decisions on the survivability of load consumers and the resilience of distribution networks. The computational findings indicate that as the deployment of MEGs gradually increases, the marginal impact of further increasing their quantity diminishes in terms of improving coverage probability and reducing load shedding. Furthermore, the proposed method outperforms other approaches in terms of required computation time.

4) The proposed analytical framework provides novel insights into studying and quantifying the structural resilience of distribution networks. Our future work will focus on its combination with state-of-the-art optimization techniques to address the performance evaluation and planning problems of large-scale power networks, considering massive potential failure scenarios.

Declaration of Competing Interest

Yunhe Hou is an associate editor for *Journal of Economy and Technology* and was not involved in the editorial review or the decision to publish this article. All authors declare that there are no competing interests.

Acknowledgment

References

Andrews, J.G., Baccelli, F., Ganti, R.K., 2011. A tractable approach to coverage and rate in cellular networks. IEEE Trans. Commun. 59 (11), 3122–3134.

Atat, R., Ismail, M., Shaaban, M.F., Serpedin, E., Overbye, T., 2020a. Stochastic geometry-based model for dynamic allocation of metering equipment in spatio-temporal expanding power grids. IEEE Trans. Smart Grid 11 (3), 2080–2091.

Atat, R., Ismail, M., Serpedin, E., Overbye, T., 2020b. Dynamic joint allocation of EV charging stations and DGs in spatio-temporal expanding grids. IEEE Access 8, 7280–7294.

Baraba´si, A.L., 2013. Network Science. Philos. Trans. R. Soc. A Math. Phys. Eng. Sci. 371 (1987), 20120375.

Baran, M.E., Wu, F.F., 1989. Network reconfiguration in distribution systems for loss reduction and load balancing. IEEE Trans. Power Deliv. 4 (2), 1401–1407.

Bessani, M., Massignan, J.A.D., Fanucchi, R.Z., Camillo, M.H.M., London, J.B.A., Delbem, A.C.B., Maciel, C.D., 2019. Probabilistic assessment of power distribution systems resilience under extreme weather. IEEE Syst. J. 13 (2), 1747–1756.

Busby, J.W., Baker, K., Bazilian, M.D., et al., 2021. Cascading risks: Understanding the 2021 winter blackout in Texas. Energy Res oc Sci. 77, 102106.

Cai, S., Xie, Y., Wu, Q., Jin, X., Zhang, M., Xiang, Z., 2023. Two-stage mobile emergency generator dispatch for sequential service restoration of microgrids in extreme conditions. Int J. Electr. Power Energy Syst. 153, 109312.

Chiu, S.N., Stoyan, D., Kendall, W.S., et al., 2013. Stochastic Geometry and Its Applications. John Wiley & Sons,.

David, H.A., Nagaraja, H.N., 2004. Order statistics. John Wiley & Sons,.

Erenog˜lu, A.K., Erdinc¸, O., 2021. Post-Event restoration strategy for coupled distribution-transportation system utilizing spatiotem- poral flexibility of mobile emergency generator and mobile energy storage system. Electr. Power Syst. Res 199, 107432.

Gao, J., Barzel, B., Baraba´si, A.L., 2016. Universal resilience patterns in complex networks. Nature 530 (7590), 307–312.

Ghasemi, S., Moshtagh, J., 2022. Distribution system restoration after extreme events considering distributed generators and static energy storage systems with mobile energy storage systems dispatch in transportation systems. Appl. Energy 310 (15), 118507.

Godsil, C., Royle, G.F., 2001. Algebraic Graph Theory. Springer Science & Business Media,.

Haenggi, M., 2012. Stochastic Geometry for Wireless Networks. Cambridge University Press,.

Hou, H., Tang, J., Zhang, Z., Wang, Z., Wei, R., Wang, L., He, H., Wu, X., 2023. Resilience enhancement of distribution network under typhoon disaster based on two-stage stochastic programming. Appl. Energy 338 (15), 120892.

IEA. Power Systems in Transition, IEA 2020.Available: https://www.iea.org/reports/power-systems-in-transition, License: CC BY 4.0.

Lagonotte, P., Sabonnadiere, J.C., Leost, J.Y., Paul, J.P., 1989. Structural analysis of the electrical system: application to secondary voltage control in France. IEEE Trans. Power Syst. 4 (2), 479–486.

Lei, S., Wang, J., Chen, C., Hou, Y., 2018. Mobile emergency generator pre-positioning and real-time allocation for resilient response to natural disasters. IEEE Trans. Smart Grid 9 (3), 2030–2041.

Mak, H.Y., Shen, Z.J.M., 2016. Integrated modeling for location analysis. Found. Trends Technol. Inf. Oper. Manag.

McGranaghan, M., Olearczyk, M., Gellings, C., 2013. Enhancing distribution resiliency: Opportunities for applying innovative technologies. Elect. Power Res Inst.

Morone, F., Makse, H.A., 2015. Influence maximization in complex networks through optimal percolation. Nature 524 (7563), 65–68.

National Academies of Sciences, Engineering, and Medicine, 2017. Enhancing the resilience of the nation's electricity system. National Academies Press,.

Pagani, G.A., Aiello, M., 2013. The Power Grid as a complex network: A survey. Phys. A: Stat. Mech. 392 (11), 2688–2700.

Panteli, M., Pickering, C., Wilkinson, S., Dawson, R., Mancarella, P., 2017. Power system resilience to extreme weather: Fragility modeling, probabilistic impact assessment, and adaptation measures. IEEE Trans. Power Syst. 32 (5), 3747–3757.

Poudel, S., Ni, Z., Sun, W., 2018. Electrical distance approach for searching vulnerable branches during contingencies. IEEE Trans. Smart Grid 9 (4), 3373–3382.

Ren, C., Hou, Y., 2022. A novel assessment method of resilient power system using stochastic geometry. Proc. IEEE Power Energy Soc. Gen. Meet. 1–5.

Ren C., Hou Y. A novel evaluation method of electric vehicles charging network based on stochastic geometry. Proc IEEE PES Innov Smart Grid Technol Conf Eur (ISGT–Eur) 2020:464–468.

Ross, S.M., 2014. Introduction to probability models. Academic press,.

Sadegh, A.R., Nazar, M.S., Shafie-khah, M., et al., 2022. Optimal resilient allocation of mobile energy storages considering coordinated microgrids biddings. Appl. Energy 328, 120117.

Scheffer, M., Carpenter, S.R., Lenton, T.M., et al., 2012. Anticipating Critical Transitions. Science 338 (6105), 344–348.

Shafieezadeh, A., Burden, L.I., 2014. Scenario-based resilience assessment framework for critical infrastructure systems: Case study for seismic resilience of seaports. Reliab Eng. Syst. Saf. 132, 207–219.

Shang, J., Sheng, X., Zhang, J.H., Zhao, W., 2009. The optimized allocation of mobile emergency generator based on the loads importance. Proc. Asia–Pac Power Energy Eng. Conf. IEEE 1–4.

Song, Y., Hill, D.J., Liu, T., 2019. On extension of effective resistance with application to graph laplacian definiteness and power network stability. IEEE Trans. Circuits Syst. I Regul. Pap. 66 (11), 4415–4428.

Wang, C., Hou, Y., Qiu, F., Lei, S., Liu, K., 2017. Resilience enhancement with sequentially proactive operation strategies. IEEE Trans. Power Syst. 32 (4), 2847–2857.

Wang, Y., Rousis, A.O., Strbac, G., 2022. Resilience-driven optimal sizing and pre-positioning of mobile energy storage systems in decentralized networked microgrids. Appl. Energy 305, 117921.

Watson, D.F., 1981. Computing the n–dimensional Delaunay tessellation with application to Voronoi polytopes. Comput. J. 24 (2), 167–172.

Wu, H., Xie, Y., Wu, Q., Yu, C., Sun, J., 2023. A three-stage resilient dispatch of mobile emergency generators in a distribution system against hurricanes. Int J. Electr. Power Energy Syst. 148, 108844.

Zhang, D., Fu, Z., Zhang, L., 2007. An improved TS algorithm for loss-minimum reconfiguration in large-scale distribution systems. Electr. Power Syst. Res 77 (5–6), 685–694.

Zhang, L., Yu, S., Zhang, B., Li, G., Cai, Y., Tang, W., 2023a. Outage management of hybrid AC/DC distribution systems: Co-optimize service restoration with repair crew and mobile energy storage system dispatch. Appl. Energy 335 (1), 120422.

Zhang, Q., Wang, Z., Ma, S., Arif, A., 2021. Stochastic pre-event preparation for enhancing resilience of distribution systems. Renew. Sustain. Energy Rev. 152, 111636.

Zhou, L., Fan, M., Zhang, Z., 2009. A study on the optimal allocation of emergency power supplies in urban electric network. Proc. 20th Int Conf. Exhib. Elect. Distrib. 1–4.